

RECEIVED: December 27, 2019

REVISED: June 15, 2020

ACCEPTED: June 19, 2020

PUBLISHED: July 17, 2020

Transverse-momentum-dependent parton distributions up to N³LL from Drell-Yan data

Alessandro Bacchetta,^{a,b} Valerio Bertone,^{a,b} Chiara Bissoletti,^{a,b} Giuseppe Bozzi,^{a,b}
Filippo Delcarro,^c Fulvio Piacenza^{a,b} and Marco Radici^b

^a*Dipartimento di Fisica, Università di Pavia,
via Bassi 6, I-27100 Pavia, Italy*

^b*INFN Sezione di Pavia,
via Bassi 6, I-27100 Pavia, Italy*

^c*Jefferson Lab,
12000 Jefferson Avenue, Newport News, Virginia 23606, U.S.A.*

E-mail: alessandro.bacchetta@unipv.it, valerio.bertone@cern.ch,
chiara.bissoletti01@universitadipavia.it, giuseppe.bozzi@unipv.it,
delcarro@jlab.org, fulvio.piacenza01@universitadipavia.it,
marco.radici@pv.infn.it

ABSTRACT: We present an extraction of unpolarised Transverse-Momentum-Dependent Parton Distribution Functions based on Drell-Yan production data from different experiments, including those at the LHC, and spanning a wide kinematic range. We deal with experimental uncertainties by properly taking into account correlations. We include re-summation of logarithms of the transverse momentum of the vector boson up to N³LL order, and we include non-perturbative contributions. These ingredients allow us to obtain a remarkable agreement with the data.

KEYWORDS: QCD Phenomenology

ARXIV EPRINT: [1912.07550](https://arxiv.org/abs/1912.07550)

Contents

1	Introduction	1
2	Theoretical framework	2
2.1	Drell-Yan cross section in TMD factorisation	3
2.2	TMD evolution and matching	5
2.3	Perturbative content	6
2.4	Logarithmic ordering	8
2.5	Non-perturbative content and its parameterisation	11
3	Experimental data	14
4	Results	19
4.1	Fit quality	19
4.2	TMD distributions	21
4.3	Perturbative convergence	23
4.4	Reduced dataset and x dependence	25
4.5	Dependence on the cut on q_T/Q	26
5	Conclusions	26
A	Numerics and delivery	28
B	Integrating over q_T	29
B.1	Kinematic cuts	30
C	Cuts on the final-state leptons	31
C.1	Azimuthally-dependent contributions	36

1 Introduction

The analysis of hard scattering processes involving nucleons in the initial state allows us to obtain information on their internal structure, encoded in parton distribution functions (PDFs).

After decades of studies, we have obtained a detailed knowledge of unpolarised collinear PDFs: they provide information about matter at the subnuclear level and are indispensable in almost any prediction involving high-energy hadrons. Collinear PDFs describe the distribution of partons inside the nucleon as a function of the longitudinal momentum fraction x . Collinear factorisation theorems lead to a precise definition of collinear PDFs based on

perturbative QCD and, within specific approximations, determine also their connection to experimental observables.

When considering semi-inclusive observables, factorisation theorems require the introduction of more general PDFs. We will focus in particular on the q_T distribution of vector bosons (γ and Z) produced in Drell-Yan processes. At low q_T , this observable can be written in terms of Transverse-Momentum-Dependent Parton Distribution Functions (TMD PDFs or, in short, TMDs), which describe the distribution of partons as a function not only of the longitudinal momentum fraction x , but also of the partonic transverse momentum k_\perp (see, e.g., refs. [1–3] and references therein). TMDs are partially computable by means of well-established perturbative methods that take into account soft and collinear radiation to all orders. However, calculations based on perturbative QCD become unreliable for values of transverse momentum close to the Landau pole (Λ_{QCD}). In this regime, non-perturbative components have to be included and have to be determined through fits to experimental data.

Several works in the past have studied the non-perturbative components in Drell-Yan q_T distributions [4–11] or in semi-inclusive DIS [12, 13], without directly mentioning TMDs. More recent works directly performed extractions of TMDs from Drell-Yan data [14–16], semi-inclusive DIS data [17, 18] or both [19–22]. Alternatively, TMDs were determined in the so-called parton-branching approach by solving evolution equations with an iterative method similar to parton showers but including transverse momentum dependence [23, 24].

A precise knowledge of TMDs is useful not only to investigate the structure of the nucleon in greater detail, but also to improve the reliability of predictions involving TMDs. At high energies, the perturbative part of TMDs may be dominant, but when extreme precision is required, also the non-perturbative components become relevant (see, e.g., ref. [25]).

In this work, we will determine the unpolarised quark TMDs by fitting Drell-Yan data from experiments at Tevatron, RHIC, LHC, and low-energy experiments at Fermilab, for a total of around 350 data points. The dataset is similar to the one studied in ref. [16], but there are some important differences: whenever available, we use cross-section measurements without any normalisation factor; TMD evolution is implemented in a different way; for the first time, TMD evolution is implemented up to next-to-next-to-next-to-leading logarithmic (N^3LL) accuracy. Compared to ref. [21], we exclude data from semi-inclusive Deep Inelastic Scattering, but we greatly extend the Drell-Yan data dataset, we improve the logarithmic accuracy, we study normalisations with much greater care, and we abandon the narrow-width approximation for Z -boson production data.

The paper is organised as follows. In section 2, we give some details of the theoretical framework. In section 3, we describe the selection of experimental data. In section 4, we show our results. Finally, in section 5 we draw our conclusions.

2 Theoretical framework

In this section we describe the theoretical framework of our analysis. In section 2.1, we review the TMD factorisation formula for the Drell-Yan (DY) process. In section 2.2, we briefly describe the evolution of TMDs and how they can be matched onto the collinear

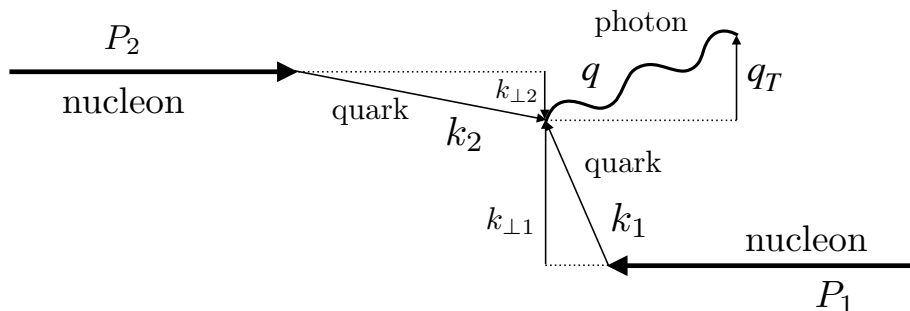


Figure 1. Diagram displaying the relevant momenta involved in a Drell-Yan event. In a reference frame in which two colliding nucleons move along the z direction with 4-momenta P_1 and P_2 , a quark with 4-momentum k_1 and transverse momentum $\mathbf{k}_{\perp 1}$ annihilates with a parton with 4-momentum k_2 and transverse momentum $\mathbf{k}_{\perp 2}$. A (virtual) photon (or Z) is produced with 4-momentum q and transverse momentum $\mathbf{q}_T = \mathbf{k}_{\perp 1} + \mathbf{k}_{\perp 2}$.

PDFs. Section 2.3 collects the perturbative ingredients of the factorised formula within the particular choice of the evolution scales adopted in this analysis. In section 2.4, we discuss how these perturbative ingredients are to be combined to achieve a given logarithmic accuracy of the resummation provided by TMD factorisation. In this context, we also review the different logarithmic-counting prescriptions used in the literature, highlighting the possible differences. Finally, in section 2.5 we motivate the introduction of a non-perturbative contribution that needs to be determined from data, and we discuss its particular functional form.

2.1 Drell-Yan cross section in TMD factorisation

In the inclusive Drell-Yan process

$$h_1(P_1) + h_2(P_2) \longrightarrow \gamma^*/Z(q) + X \longrightarrow \ell^+(l) + \ell^-(l') + X, \quad (2.1)$$

two hadrons h_1 and h_2 with 4-momenta P_1 and P_2 , respectively, collide with center-of-mass energy squared $s = (P_1 + P_2)^2$ and produce a neutral vector boson γ^*/Z with 4-momentum q and large invariant mass $Q = \sqrt{q^2}$. The vector boson eventually decays into a lepton and an antilepton with 4-momenta constrained by momentum conservation, $q = l + l'$. The absolute value of the transverse momentum and the rapidity of the neutral boson (or, equivalently, of the lepton pair) are defined as

$$q_T = \sqrt{q_x^2 + q_y^2}, \quad y = \frac{1}{2} \ln \left(\frac{q_0 + q_z}{q_0 - q_z} \right), \quad (2.2)$$

where the z direction is defined by the hadronic-collision axis (see figure 1).

We are specifically interested in the transverse-momentum distribution of the vector boson in the small- q_T region ($q_T \ll Q$). In this regime, the (unpolarised) differential cross section factorises and can be expressed in terms of the (unpolarised) TMDs of the two

hadrons as

$$\frac{d\sigma}{dQdydq_T} = \frac{16\pi^2\alpha^2q_T\mathcal{P}}{9Q^3}H(Q,\mu)\sum_q c_q(Q) \times \int d^2\mathbf{k}_{\perp 1}d^2\mathbf{k}_{\perp 2}x_1f_1^q(x_1,\mathbf{k}_{\perp 1};\mu,\zeta_1)x_2f_1^{\bar{q}}(x_2,\mathbf{k}_{\perp 2};\mu,\zeta_2)\delta^{(2)}(\mathbf{k}_{\perp 1}+\mathbf{k}_{\perp 2}-\mathbf{q}_T), \quad (2.3)$$

where α is the electromagnetic coupling and \mathcal{P} is the phase-space reduction factor due to possible kinematic cuts on the final-state leptons (see appendix C).¹ The hard factor H represents the perturbative part of the hard scattering and depends on the hard scale Q and on the renormalisation scale μ . The summation over q in eq. (2.3) runs over the active quarks and antiquarks at the scale Q , and c_q are the respective electroweak charges given by

$$c_q(Q) = e_q^2 - 2e_qV_qV_\ell\chi_1(Q) + (V_\ell^2 + A_\ell^2)(V_q^2 + A_q^2)\chi_2(Q), \quad (2.4)$$

with

$$\chi_1(Q) = \frac{1}{4\sin^2\theta_W\cos^2\theta_W}\frac{Q^2(Q^2 - M_Z^2)}{(Q^2 - M_Z^2)^2 + M_Z^2\Gamma_Z^2}, \quad (2.5)$$

$$\chi_2(Q) = \frac{1}{16\sin^4\theta_W\cos^4\theta_W}\frac{Q^4}{(Q^2 - M_Z^2)^2 + M_Z^2\Gamma_Z^2}, \quad (2.6)$$

where e_q , V_q , and A_q are respectively the electric, vector, and axial charges of the flavour q ; V_ℓ and A_ℓ are the vector and axial charges of the lepton ℓ ; $\sin\theta_W$ is the weak mixing angle; M_Z and Γ_Z are mass and width of the Z boson.

The second line of eq. (2.3) displays the convolution of the TMDs f_1^q and $f_1^{\bar{q}}$ of the hadrons h_1 and h_2 , respectively. It describes the annihilation of a quark q , with longitudinal momentum fraction $x_1 = Qe^y/\sqrt{s}$ and transverse momentum $\mathbf{k}_{\perp 1}$, with the corresponding antiquark \bar{q} , with longitudinal momentum fraction $x_2 = Qe^{-y}/\sqrt{s}$ and transverse momentum $\mathbf{k}_{\perp 2}$. In the annihilation, the momentum conservation is guaranteed by the presence of $\delta^{(2)}(\mathbf{k}_{\perp 1} + \mathbf{k}_{\perp 2} - \mathbf{q}_T)$ (see figure 1).

As a consequence of renormalisation and of the removal of the rapidity divergences [27], TMDs acquire a dependence on the renormalisation scale μ and on the so-called rapidity scale ζ . We will discuss our choice for these scales in section 2.3. Here, we just remark that the rapidity scales ζ_1 and ζ_2 in eq. (2.3) must obey the kinematic constraint $\zeta_1\zeta_2 = Q^4$.

It is convenient to rewrite the convolution in the conjugate position space by using the Fourier transform of each TMD, defined as²

$$\hat{f}_1^q(x, b_T; \mu, \zeta) = \int d^2\mathbf{k}_{\perp}e^{i\mathbf{k}_{\perp}\cdot\mathbf{b}_T}f_1^q(x, \mathbf{k}_{\perp}^2; \mu, \zeta), \quad (2.7)$$

¹In the presence of cuts on single lepton variables, an additional parity-violating term contributes to the cross section [26]. However, in appendix C we argue that this contribution is negligible in the experimental conditions considered in this paper.

²For simplicity, in the rest of the paper we will refer to the b_T -dependent function \hat{f}_1 as to TMD but understanding that this is in fact the Fourier transform of the actual TMD f_1 . Note that in ref. [21] the variable ξ_T was used in place of b_T . The reason was to avoid confusion with the impact parameter used in the GPD literature for which the symbol b_T is typically used. In this paper, we decided to use b_T as it is more common in the TMD, q_T -resummation, and SCET literature but keeping in mind that this is *not* the impact parameter but the Fourier conjugate variable of q_T . Finally, we notice that in ref. [21] the Fourier transform was defined with an extra $1/(2\pi)$ factor.

where b_T is the absolute value of the vector \mathbf{b}_T ($b_T = |\mathbf{b}_T|$). By using eq. (2.7), we can rewrite the convolution of TMDs as

$$\begin{aligned}
 & \int d^2\mathbf{k}_{\perp 1} d^2\mathbf{k}_{\perp 2} x_1 f_1^q(x_1, \mathbf{k}_{\perp 1}^2; \mu, \zeta_1) x_2 f_1^{\bar{q}}(x_2, \mathbf{k}_{\perp 2}^2; \mu, \zeta_2) \delta^{(2)}(\mathbf{k}_{\perp 1} + \mathbf{k}_{\perp 2} - \mathbf{q}_T) \\
 &= \int \frac{d^2\mathbf{b}_T}{(2\pi)^2} e^{i\mathbf{b}_T \cdot \mathbf{q}_T} x_1 \hat{f}_1^q(x_1, b_T; \mu, \zeta_1) x_2 \hat{f}_1^{\bar{q}}(x_2, b_T; \mu, \zeta_2) \\
 &= \frac{1}{2\pi} \int_0^\infty db_T b_T J_0(b_T q_T) x_1 \hat{f}_1^q(x_1, b_T; \mu, \zeta_1) x_2 \hat{f}_1^{\bar{q}}(x_2, b_T; \mu, \zeta_2),
 \end{aligned} \tag{2.8}$$

where J_0 is the 0-th order Bessel function of the first kind that has the following integral representation

$$J_0(x) = \frac{1}{2\pi} \int_0^{2\pi} d\theta e^{ix \cos \theta}. \tag{2.9}$$

By inserting eq. (2.8) into the cross section in eq. (2.3), we finally get

$$\begin{aligned}
 \frac{d\sigma}{dQ dy dq_T} &= \frac{8\pi\alpha^2 q_T \mathcal{P}}{9Q^3} H(Q, \mu) \\
 &\times \sum_q c_q(Q) \int_0^\infty db_T b_T J_0(b_T q_T) x_1 \hat{f}_1^q(x_1, b_T; \mu, \zeta_1) x_2 \hat{f}_1^{\bar{q}}(x_2, b_T; \mu, \zeta_2),
 \end{aligned} \tag{2.10}$$

which is the formula actually implemented in our analysis of Drell-Yan data.

2.2 TMD evolution and matching

In eq. (2.10), the dependence of the TMDs $\hat{f}_1^{q(\bar{q})}$ on the scales μ and ζ arises from the removal of the ultraviolet and rapidity divergences in their operator definition. Each dependence is controlled by an evolution equation:

$$\frac{\partial \ln \hat{f}_1}{\partial \ln \mu} = \gamma(\mu, \zeta), \quad \frac{\partial \ln \hat{f}_1}{\partial \ln \sqrt{\zeta}} = K(\mu), \tag{2.11}$$

where γ is the anomalous dimension of the Renormalisation Group (RG) evolution in μ , and K is the anomalous dimension of the Collins-Soper evolution in $\sqrt{\zeta}$ [28]. Notice that, for brevity, we have dropped the flavour index q and \bar{q} . Moreover, since in this section we will only be concerned with the dependence of \hat{f}_1 on the scales μ and ζ , we will also temporarily drop the dependence on x and b_T . In addition to the evolution equations in eq. (2.11), the rapidity anomalous dimension K obeys its own RG equation:

$$\frac{\partial K}{\partial \ln \mu} = -\gamma_K(\alpha_s(\mu)), \tag{2.12}$$

where γ_K is known as cusp anomalous dimension. Since the crossed double derivatives of \hat{f}_1 must be equal, using eqs. (2.11) and (2.12) we also get

$$\frac{\partial \gamma}{\partial \ln \sqrt{\zeta}} = -\gamma_K(\alpha_s(\mu)). \tag{2.13}$$

Using the point $\zeta = \mu^2$ as a boundary condition, the solution of this differential equation is

$$\gamma(\mu, \zeta) = \gamma_F(\alpha_s(\mu)) - \gamma_K(\alpha_s(\mu)) \ln \frac{\sqrt{\zeta}}{\mu}, \quad (2.14)$$

where $\gamma_F(\alpha_s(\mu)) \equiv \gamma(\mu, \mu^2)$. If the TMD \hat{f}_1 is known at some starting scales μ_0 and ζ_0 , the solution of the evolution equations in eq. (2.11) reads

$$\hat{f}_1(\mu, \zeta) = R[(\mu, \zeta) \leftarrow (\mu_0, \zeta_0)] \hat{f}_1(\mu_0, \zeta_0), \quad (2.15)$$

where the so-called Sudakov form factor R accounts for the perturbative evolution of \hat{f}_1 and it is defined as

$$R[(\mu, \zeta) \leftarrow (\mu_0, \zeta_0)] = \exp \left\{ K(\mu_0) \ln \frac{\sqrt{\zeta}}{\sqrt{\zeta_0}} + \int_{\mu_0}^{\mu} \frac{d\mu'}{\mu'} \left[\gamma_F(\alpha_s(\mu')) - \gamma_K(\alpha_s(\mu')) \ln \frac{\sqrt{\zeta}}{\mu'} \right] \right\}. \quad (2.16)$$

We note that eq. (2.16) can be implemented in various ways [29–32]. In this work, we follow the standard approach described in [27]. Moreover, we calculate all ingredients involved in eq. (2.16) by adopting a fully numerical approach.

An important property of the TMD \hat{f}_1 is that at small values of b_T it can be matched onto the *collinear* PDF f_1 . Reinstating for clarity the x and b_T dependence and introducing the matching coefficient function C , we can write³

$$\hat{f}_1(x, b_T; \mu_0, \zeta_0) = \int_x^1 \frac{dy}{y} C(y, b_T; \mu_0, \zeta_0) f_1\left(\frac{x}{y}; \mu_0\right) \equiv [C \otimes f_1](x, b_T; \mu_0, \zeta_0). \quad (2.17)$$

Then, the actual evolved TMD becomes

$$\hat{f}_1(x, b_T; \mu, \zeta) = R[b_T; (\mu, \zeta) \leftarrow (\mu_0, \zeta_0)] [C \otimes f_1](x, b_T; \mu_0, \zeta_0). \quad (2.18)$$

2.3 Perturbative content

In order to use eq. (2.18) in phenomenological applications, we need to define the values of both the initial and final pairs of scales, (μ_0, ζ_0) and (μ, ζ) . It turns out that in the $\overline{\text{MS}}$ renormalisation scheme there exists a particular scale,

$$\mu_b(b_T) = \frac{2e^{-\gamma_E}}{b_T}, \quad (2.19)$$

with γ_E the Euler constant, such that the rapidity anomalous dimension K and the matching coefficient C computed at $\mu_0 = \sqrt{\zeta_0} = \mu_b$ admit a pure perturbative expansion free of explicit logarithms of the scales. Therefore, μ_b provides a natural choice for μ_0 and $\sqrt{\zeta_0}$.

The final renormalisation scale μ must match the one used in the hard factor H in eq. (2.10). Therefore, μ has to be of order Q for avoiding large logarithms in H : we choose $\mu = Q$. Any variation of μ with respect to this choice can be accounted for by expanding the solution of the RG equation for the strong coupling α_s . The rapidity scales ζ_1 and

³A sum over flavours is understood. The matching function C has to be regarded as a matrix in flavour space multiplying a column vector of collinear PDFs.

ζ_2 in eq. (2.10) are bound to comply with $\zeta_1\zeta_2 = Q^4$. Therefore, the natural choice is $\zeta_1 = \zeta_2 = Q^2$. However, we stress that any choice that fulfils this constraint leads to the same cross section. In fact, from eq. (2.16) it should be evident that the evolution factors R entering the two TMDs in eq. (2.10) combine in such a way that the result only depends on the product $\zeta_1\zeta_2$.

After choosing the scales, we discuss the perturbative ingredients that result from this particular choice. We first consider the hard function H . Up to two-loop accuracy, its perturbative expansion is

$$H(Q, Q) = 1 + \sum_{n=1}^2 \left(\frac{\alpha_s(Q)}{4\pi} \right)^n H^{(n)}. \quad (2.20)$$

The coefficients $H^{(n)}$ can be read off from, *e.g.*, ref. [33]. When going beyond $\mathcal{O}(\alpha_s^2)$, the hard function acquires a non-trivial flavour structure (see, *e.g.*, ref. [34]). As a consequence, H should in principle be moved inside the flavour sum in eq. (2.10). However, in the present analysis we do not consider corrections beyond $\mathcal{O}(\alpha_s^2)$ and eq. (2.10) is appropriate.

Next, we consider the matching function C introduced in eq. (2.17). By making the flavour and x dependences explicit, the C have the following perturbative expansion

$$C_{ij}(x, b_T; \mu_b, \mu_b^2) = \delta_{ij}\delta(1-x) + \sum_{n=1}^{\infty} \left(\frac{\alpha_s(\mu_b)}{4\pi} \right)^n C_{ij}^{(n)}(x). \quad (2.21)$$

The coefficient functions $C_{ij}^{(n)}$ up to $n = 2$ have been computed in refs. [35, 36]. They have been reported also in ref. [34], where the authors have verified the consistency of the results. The calculation of the $\mathcal{O}(\alpha_s^3)$ corrections to the quark matching functions appeared very recently in ref. [37].

As for the anomalous dimensions K , γ_F , and γ_K in the Sudakov form factor in eq. (2.16), their perturbative expansions read, respectively,

$$\begin{aligned} K(\mu_b) &= \sum_{n=0}^{\infty} \left(\frac{\alpha_s(\mu_b)}{4\pi} \right)^{n+1} K^{(n)}, \\ \gamma_F(\alpha_s(\mu)) &= \sum_{n=0}^{\infty} \left(\frac{\alpha_s(\mu)}{4\pi} \right)^{n+1} \gamma_F^{(n)}, \\ \gamma_K(\alpha_s(\mu)) &= \sum_{n=0}^{\infty} \left(\frac{\alpha_s(\mu)}{4\pi} \right)^{n+1} \gamma_K^{(n)}. \end{aligned} \quad (2.22)$$

The coefficients $K^{(n)}$ are listed up to $n = 3$ in ref. [36] and up to $n = 2$ in ref. [34]. They differ by a factor -2 due to a different definition of K . Also the coefficients $\gamma_F^{(n)}$ are given in refs. [34, 36] up to $n = 2$, and they differ by a minus sign due to a different definition of the anomalous dimension. Finally, the coefficients $\gamma_K^{(n)}$ were originally computed in ref. [38] and are also given in refs. [34, 36] up to $n = 2$, where they differ by a factor 2. The coefficient $\gamma_K^{(3)}$ has been recently computed in refs. [39–41].

2.4 Logarithmic ordering

In this section, we discuss how to combine in a consistent way the perturbative ingredients of eqs. (2.20)–(2.22) for the computation of the cross section in eq. (2.10) (see also refs. [42, 43]).

As is well known, TMD factorisation provides resummation of large logarithms of Q/q_T or, equivalently, of Q/μ_b . The resummation is implemented in the Sudakov form factor R in eq. (2.16) whose perturbative expansion reads

$$R = 1 + \sum_{n=1}^{\infty} \left(\frac{\alpha_s(Q)}{4\pi} \right)^n \sum_{k=1}^{2n} L^k R^{(n,k)}, \quad (2.23)$$

with

$$L = \ln \frac{Q^2}{\mu_b^2}. \quad (2.24)$$

Because of the inner sum running up to $2n$, eq. (2.23) exposes the double-logarithmic nature of the resummation. This structure can be traced back to the evolution equations in eq. (2.11) that resum *two different* categories of logarithms. However, our particular choice of the scales ($\mu_0 = \sqrt{\zeta_0} = \mu_b$ and $\mu = \sqrt{\zeta} = Q$) makes the two categories to coincide, producing up to two logarithms for each power of α_s . Consequently, eq. (2.23) must include all powers of α_s if the scales are such that $\alpha_s L^2 \gtrsim 1$.

The expansion (2.23) can be rearranged to define a logarithmic ordering as

$$R = 1 + \sum_{k=0}^{\infty} R_{\text{N}^k\text{LL}}, \quad (2.25)$$

with

$$R_{\text{N}^k\text{LL}} = \sum_{n=1+[k/2]}^{\infty} \left(\frac{\alpha_s(Q)}{4\pi} \right)^n L^{2n-k} R^{(n,2n-k)}, \quad (2.26)$$

where $[k/2]$ is the integer part of $k/2$. According to this definition, the term $k = 0$ in eq. (2.25) gives the leading-logarithmic (LL) approximation, the term $k = 1$ gives the next-to-leading-logarithmic (NLL) approximation, and so on. Multiplication of $R_{\text{N}^k\text{LL}}$ by a power p of α_s gives

$$\left(\frac{\alpha_s(Q)}{4\pi} \right)^p R_{\text{N}^k\text{LL}} = \sum_{m=1+[(k+2p)/2]}^{\infty} \left(\frac{\alpha_s(Q)}{4\pi} \right)^m L^{2m-(k+2p)} R^{(m-p,2m-(k+2p))} \sim R_{\text{N}^{k+2p}\text{LL}}, \quad (2.27)$$

where the symbol \sim means that the left- and right-hand sides have the same logarithmic accuracy. This step is relevant because in the cross section the Sudakov form factor, eq. (2.25), can be multiplied by some power of α_s originating from the hard factor H and/or the matching functions C . Equation (2.27) states that, at the cross section level, the inclusion of an additional power of α_s in the perturbative expansion of H and/or C implies a contribution two orders higher with respect to the leading term in the logarithmic expansion. For example, at LL and NLL accuracy the functions H and C can be computed

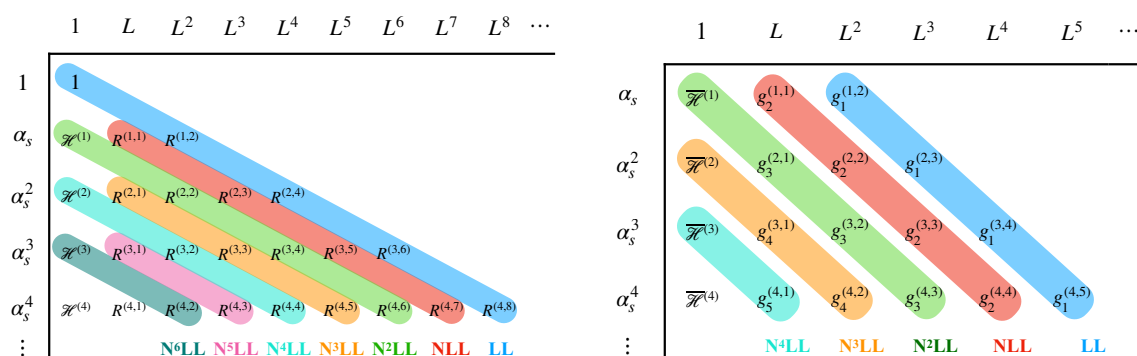


Figure 2. Graphical representation of logarithmic countings: in the left panel the counting is done at the level of the cross section, in the right panel at the level of the logarithm of the cross section.

at $\mathcal{O}(1)$, at NNLL and N³LL they need to include the $\mathcal{O}(\alpha_s)$ corrections, and so on. This logarithmic counting is illustrated in the left panel of figure 2: the diagonal bands represent the terms included in each $R_{N^k LL}$, with $\mathcal{H}^{(n)}$ the perturbative coefficients of either H or C or a combination of the two.

The counting discussed above generally applies to any process whose amplitude factorises in the appropriate limit, such as DY in the $q_T \ll Q$ limit (TMD factorisation). However, in the specific case of DY (i.e., inclusive with respect to soft-collinear QCD radiation) also the phase space for the emission of n real particles in b_T space factorises (see, e.g., ref. [44]). This feature, along with the factorisation of the amplitude in the $q_T \ll Q$ limit, allows one to *exponentiate* soft-collinear emissions such that the Sudakov form factor can be written in the following general form (see, e.g., ref. [45])⁴

$$R = \exp \left[\frac{1}{2} L g^{(1)}(\alpha_s L) + \frac{1}{2} g^{(2)}(\alpha_s L) + \frac{1}{2} \alpha_s g^{(3)}(\alpha_s L) + \dots \right], \quad (2.28)$$

where the functions $g^{(i)}$ are such that $g^{(i)}(0) = 0$. As compared to the general counting in eq. (2.23), exponentiation relates all the terms in eq. (2.23) of the type $\alpha_s^n L^m$ with $n + 1 < m \leq 2n$ to the lower-order terms. In eq. (2.28), the logarithmic counting is performed at the level of the argument of the exponential. In this context, the terms $Lg^{(1)}$, $g^{(2)}$, $\alpha_s g^{(3)}$, etc., resum, respectively, the LL contributions $\alpha_s^n L^{n+1}$, the NLL contributions $\alpha_s^n L^n$, the NNLL contributions $\alpha_s^n L^{n-1}$, etc.. Contrary to eq. (2.23), this counting is driven by the condition $\alpha_s L \gtrsim 1$. This extends the validity of the resummed result (truncated at a given level: NLL, NNLL, etc.) to larger values of L (smaller values of q_T/Q).

The logarithmic counting applied to the argument of the exponential is equivalent to consider the logarithm of the cross section [33]. In fact, neglecting for simplicity the matching functions, we schematically have

$$\ln \left(\frac{d\sigma}{dQ dy dq_T} \right) \propto \ln H + Lg^{(1)} + g^{(2)} + \alpha_s g^{(3)} + \dots \quad (2.29)$$

⁴The factors 1/2 in the argument of the exponential are justified by the fact that each of the two TMDs involved in the DY cross section contains an evolution factor R . In this way, eq. (2.28) matches the literature on q_T -resummation where the Sudakov form factor is usually defined as the combination of both R 's.

The logarithm of H can be expanded as

$$\ln(1 + \alpha_s H^{(1)} + \alpha_s^2 H^{(2)}) = \alpha_s H^{(1)} + \alpha_s^2 \left(H^{(2)} - \frac{H^{(1)2}}{2} \right) + \mathcal{O}(\alpha_s^3). \quad (2.30)$$

The first term $\alpha_s H^{(1)}$ contributes to the tower $\alpha_s^n L^{n-1}$, that is the NNLL contribution. The second term $\alpha_s^2 (H^{(2)} - H^{(1)2}/2)$ contributes to the $\alpha_s^n L^{n-2}$ tower, thus to the N³LL contribution. The same counting applies to the matching functions C . The conclusion is that including $\mathcal{O}(\alpha_s)$ contributions in H and C implies introducing NNLL corrections, $\mathcal{O}(\alpha_s^2)$ contributions in H and C contribute to N³LL accuracy, and so on. A graphical representation of this counting is sketched in the right panel of figure 2. Again, the bands represent the logarithmic towers, while $\overline{\mathcal{H}}^{(n)}$ are the appropriate coefficients of the expansion of either $\ln H$ or $\ln C$ or a combination. This logarithmic counting has been used in several papers (see, e.g., refs. [10, 33, 46, 47]). In this work, we will simply denote this counting with the acronyms NLL, NNLL, and so on, and for convenience we will refer to it as to “standard counting”.

A slightly different counting has also been widely used in the literature (see, e.g., refs. [42, 48–51]). Expanding the Sudakov form factor (2.28) and multiplying it by the expansion of the hard function in eq. (2.20), we obtain for the cross section

$$\frac{d\sigma}{dQdydq_T} \propto 1 + Lg^{(1)} + g^{(2)} + H^{(1)}\alpha_s Lg^{(1)} + \dots, \quad (2.31)$$

where the rightmost term stems from the combination of the first-order terms $\alpha_s H^{(1)}$ and $Lg^{(1)}$ in both expansions. As it is clear from the previous discussion, this term has the same form $\alpha_s^n L^n$ as $g^{(2)}$. Then one can argue that NLL accuracy requires the inclusion not only of $g^{(2)}$ but also of $H^{(1)}$ [48]. This argument works to all orders: at any given logarithmic accuracy, it prescribes to include one more order in the perturbative expansion of H (and/or C) with respect to the standard counting. We will refer to this counting as the to “primed counting”, denoting it as NLL’, NNLL’, and so on. The apparent contradiction between the standard and primed countings is resolved by observing that the first term of the perturbative expansion of $\alpha_s Lg^{(1)}$ is proportional to $\alpha_s^2 L^2$. When considering the general expansion of the cross section given in eqs. (2.25)–(2.27), a term proportional to $\alpha_s^2 L^2$ is of the form $\alpha_s^n L^{2n-2}$ and thus belongs to the NNLL tower. This is formally subleading with respect to the NLL accuracy determined by the $g^{(2)}$ term in the exponent.

Accurate predictions over a wide range in q_T require matching resummed calculations (valid at $q_T \ll Q$) to the corresponding fixed-order calculation (valid at $q_T \lesssim Q$). In this context, the primed ordering turns out to be more advantageous. Indeed, the accuracy of a fixed-order calculation is measured in terms of powers of α_s relative to the leading term. In order to produce a Z boson with large q_T , it is necessary to produce (at least) a second object with large transverse momentum against which the Z boson recoils, i.e., a jet. As a consequence, the leading-order (LO) contribution to the q_T distribution of the Z at fixed order is $\mathcal{O}(\alpha_s)$. The NLL’ prescription correctly reproduces the small- q_T limit of the LO fixed-order calculation. It is then possible to realise the matching in an *additive* way by

Accuracy	H and C	K and γ_F	γ_K	PDF and α_s evolution
LL	0	–	1	–
NLL	0	1	2	LO
NLL'	1	1	2	NLO
NNLL	1	2	3	NLO
NNLL'	2	2	3	NNLO
N ³ LL	2	3	4	NNLO

Table 1. Truncation order in the expansions of eqs. (2.20)–(2.22) for the two logarithmic countings considered in this paper (see text). The last column reports the order used for the evolution of the collinear PDFs and α_s .

combining the NLL' resummed calculation with the LO fixed-order one (NLL' + LO). The procedure can be extended to higher orders: NNLL' + NLO, N³LL' + NNLO, and so on. Conversely, in the standard counting the matching to the LO fixed-order calculation requires to go further to NNLL accuracy (NNLL + LO), combining in this way a rather accurate calculation at small q_T with a poorly accurate calculation at large q_T . At higher orders one has N³LL + NLO, N⁴LL + NNLO, and so on. We remark that other forms of matching can be used to overcome the limitation of the standard counting [33, 52, 53].

Finally, table 1 summarises the perturbative ingredients to be used for a consistent computation of the cross section in eq. (2.10) for both the standard and the primed countings. The numbers in table 1 give the maximum power of α_s at which the corresponding quantity is to be computed, while the last column reports the corresponding accuracy in computing the evolution of the collinear PDFs and of the coupling α_s .⁵ In this analysis, we have used the PDF sets of the MMHT2014 family [54] at the appropriate perturbative order accessed through the LHAPDF interface [55].

2.5 Non-perturbative content and its parameterisation

In the previous section, we noticed that in the $\overline{\text{MS}}$ scheme the rapidity evolution kernel K and the matching functions C can be made free of logarithms of the scales by introducing the natural scale μ_b defined in eq. (2.19). Consistently, in the perturbative expansion of K (see first line of eq. (2.22)) and C (see eq. (2.21)) the strong coupling α_s must be computed at μ_b . For large values of b_T , μ_b becomes small such that $\alpha_s(\mu_b)$ may potentially become very large and eventually diverge when μ_b reaches the Landau pole at Λ_{QCD} . As a matter of fact, the integral in eq. (2.10) does require accessing large values of b_T . It is then necessary to regularise this divergence by introducing a *prescription* that avoids integrating over the Landau pole. Different possibilities are available (see, e.g., refs. [53, 56]). In this paper, we adopt the prescription originally proposed in ref. [57]: we introduce the *arbitrary*

⁵In the “unprimed” counting, α_s is evolved at one loop less than the cusp anomalous dimensions for two reasons: first, the running coupling renormalization group equation resums single logs, therefore the β function can be taken at the same order as the non-cusp anomalous dimension. Secondly, in our analysis for consistency we take α_s from the LHAPDF grid of the PDF set we use.

parameter b_{\max} that denotes the maximum value of b_T at which perturbation theory is considered reliable. Hence, b_{\max} must be such that

$$\alpha_s \left(\frac{2e^{-\gamma_E}}{b_{\max}} \right) \ll 1. \tag{2.32}$$

Moreover, we also want to prevent μ_b from becoming much larger than the hard scale Q ($\mu_b \gg Q$). Despite not strictly mandatory (especially when considering only small values of q_T), this feature makes it possible to expand the cross section integrated in q_T , with the lowest-order term reproducing the lowest-order collinear result [58]. To this end, we define

$$b_{\min} = \frac{2e^{-\gamma_E}}{Q}, \tag{2.33}$$

and introduce a monotonic function $b_*(b_T)$ with the following asymptotic behaviours

$$\begin{aligned} b_*(b_T) &\rightarrow b_{\min} \quad \text{for } b_T \rightarrow 0, \\ b_*(b_T) &\rightarrow b_{\max} \quad \text{for } b_T \rightarrow \infty. \end{aligned} \tag{2.34}$$

In this analysis, we adopt for $b_*(b_T)$ the same functional form chosen in ref. [21] that guarantees a smooth and rapid convergence towards the asymptotic limits:

$$b_*(b_T) = b_{\max} \left(\frac{1 - \exp\left(-\frac{b_T^4}{b_{\max}^4}\right)}{1 - \exp\left(-\frac{b_T^4}{b_{\min}^4}\right)} \right)^{\frac{1}{4}}. \tag{2.35}$$

Now, we simply write the TMD \hat{f}_1 as

$$\begin{aligned} \hat{f}_1(x, b_T; \mu, \zeta) &= \left[\frac{\hat{f}_1(x, b_T; \mu, \zeta)}{\hat{f}_1(x, b_*(b_T); \mu, \zeta)} \right] \hat{f}_1(x, b_*(b_T); \mu, \zeta) \\ &\equiv f_{\text{NP}}(x, b_T, \zeta) \hat{f}_1(x, b_*(b_T); \mu, \zeta). \end{aligned} \tag{2.36}$$

This separation effectively defines f_{NP} . The advantage is that, due to the behaviour of $b_*(b_T)$ for large values of b_T , $\hat{f}_1(x, b_*(b_T), \mu, \zeta)$ remains in the perturbative region. The non-perturbative contributions are instead confined into f_{NP} , that has to be determined through a fit to experimental data. However, using eq. (2.36), we can work out some general properties of f_{NP} . First, f_{NP} does not depend on the renormalisation scale μ . To see this, using eqs. (2.15) and (2.16) with $\mu_0 = \sqrt{\zeta_0} = \mu_b$, we find

$$\begin{aligned} f_{\text{NP}}(x, b_T, \zeta) &= \frac{\hat{f}_1(x, b_T; \mu, \zeta)}{\hat{f}_1(x, b_*(b_T); \mu, \zeta)} = \exp \left\{ K(\mu_b) \ln \frac{\sqrt{\zeta}}{\mu_b} - K(\mu_{b_*}) \ln \frac{\sqrt{\zeta}}{\mu_{b_*}} \right. \\ &\quad \left. + \int_{\mu_b}^{\mu_{b_*}} \frac{d\mu'}{\mu'} \left[\gamma_F(\alpha_s(\mu')) - \gamma_K(\alpha_s(\mu')) \ln \frac{\sqrt{\zeta}}{\mu'} \right] \right\} \frac{\hat{f}_1(x, b_T; \mu_b, \mu_b^2)}{\hat{f}_1(x, b_*(b_T); \mu_{b_*}, \mu_{b_*}^2)}, \end{aligned} \tag{2.37}$$

with $\mu_{b_*} \equiv \mu_b(b_*(b_T))$. The dependence on μ evidently cancels in the ratio. In addition, for large values of b_T μ_{b_*} saturates to some minimal value while μ_b becomes increasingly

small. As a consequence of this departure between μ_{b_*} and μ_b , as well as between $\sqrt{\zeta}$ and μ_b , the exponential in eq. (2.37) tends to be suppressed, and so does f_{NP} . Conversely, as b_T becomes small b_* approaches b_{min} . Using the definition in eq. (2.33), it follows that μ_{b_*} saturates to Q while μ_b becomes larger and larger. In this limit, we have [58]

$$f_{\text{NP}} \xrightarrow{b_T \rightarrow 0} 1 + \mathcal{O}\left(\frac{1}{Q^p}\right), \quad (2.38)$$

where p is some positive number. Since TMD factorisation applies to leading-power in q_T/Q , we can neglect the power suppressed contribution such that $f_{\text{NP}} \rightarrow 1$ for $b_T \rightarrow 0$. It is important to stress that the separation between perturbative and non-perturbative components of a TMD is *arbitrary* and depends on the particular choice of b_* (or in general on the prescription used to regularise the Landau pole). For any given choice, only the combination in eq. (2.36) is meaningful, and it is misleading to refer to f_{NP} as to the non-perturbative part of TMDs in a universal sense.

Following the requirements discussed above, we parameterise f_{NP} as

$$f_{\text{NP}}(x, b_T, \zeta) = \left[\frac{1 - \lambda}{1 + g_1(x) \frac{b_T^2}{4}} + \lambda \exp\left(-g_{1B}(x) \frac{b_T^2}{4}\right) \right] \times \exp\left[-(g_2 + g_{2B} b_T^2) \ln\left(\frac{\zeta}{Q_0^2}\right) \frac{b_T^2}{4}\right], \quad (2.39)$$

with $Q_0 = 1 \text{ GeV}$ and with the $g_1(x)$ and $g_{1B}(x)$ functions given by

$$\begin{aligned} g_1(x) &= \frac{N_1}{x\sigma} \exp\left[-\frac{1}{2\sigma^2} \ln^2\left(\frac{x}{\alpha}\right)\right], \\ g_{1B}(x) &= \frac{N_{1B}}{x\sigma_B} \exp\left[-\frac{1}{2\sigma_B^2} \ln^2\left(\frac{x}{\alpha_B}\right)\right]. \end{aligned} \quad (2.40)$$

There are a total of 9 free parameters ($\lambda, g_2, g_{2B}, N_1, \sigma, \alpha, N_{1B}, \sigma_B, \alpha_B$) to be determined from data.

Apart from the logarithmic dependence on ζ , the functional form (2.39) is motivated by empirical considerations. The first line parameterises the “intrinsic” TMD non-perturbative contribution and it only depends on x and b_T . The second line accounts for the non-perturbative correction to the perturbative evolution. Therefore, it only depends on b_T (on top of the known dependence on ζ).

The intrinsic contribution is a combination of a q -Gaussian (or Tsallis) distribution (first term) and a standard Gaussian distribution (second term). The q -Gaussian has a larger tail than the standard Gaussian, meaning that it gives a bigger contribution to the TMD at small transverse momentum. We found that this combination is able to reproduce the behaviour at very small q_T of the experimental distributions from the lowest to the highest energies considered in our analysis.

The functions g_1 and g_{1B} in eq. (2.40) are related to the width of the TMD distribution. They are expected to depend on x on the basis of model calculations (see ref. [59] and references therein) and more generally from Lorentz invariance constraints on the proton

light-front wave functions (see, e.g., the discussion in ref. [60]). To best describe experimental data, we found it necessary to have wider TMDs at intermediate x . A log-normal dependence of g_1 and g_{1B} allowed us to properly describe the datasets differential in the boson rapidity y . In fact, as we will show below, the x dependence of f_{NP} is almost entirely determined by the ATLAS datasets, the only ones differential in y . Our present results are quite different from the ones obtained through fits to semi-inclusive DIS data [21]. We expect that the addition of further datasets from DIS experiments [61, 62] will provide more sensitivity to the x dependence and possibly lead to different results.

The non-perturbative components of the TMDs could depend also on flavour [17, 25, 63]. However, in this work we refrain from including such dependence since DY data are not very sensitive to it. We stress that the fact that we can achieve a good description of data does not exclude the presence of a flavour dependence, which is actually expected on the basis of model calculations [64–69], lattice QCD studies [70], and also if QED corrections are taken into account [71, 72]. Higher sensitivity to flavour dependence may be provided again by semi-inclusive DIS data with different targets and final-state hadrons and possibly by W -boson production data [73].

Concerning the b_T dependence of the non-perturbative evolution in the second line of eq. (2.39), we have used a customary quadratic term [4, 8, 12, 74] with an additional quartic term. The latter contribution appears to be useful to reproduce the energy evolution displayed by the data. Other choices of the functional form have been discussed in, e.g., refs. [20, 75–77]. This contribution could be also determined using lattice QCD [78].

3 Experimental data

In this section we describe the experimental data included in this analysis. We considered q_T distributions in DY production from a variety of datasets. Some of these were already included in the analysis of ref. [21], i.e. data from: E605 [79], E288 [80], CDF Run I [81] and Run II [82], and D0 Run I [83] and Run II [84]. We refer the reader to ref. [21] for more details. The new datasets included in the present analysis are:

- $Z \rightarrow \mu^+ \mu^-$ distribution from D0 Run II [85],
- forward Z -production data from the LHCb experiment at 7 [85], 8 [86], and 13 [87] TeV,
- Z -production data from the CMS experiment at 7 [88] and 8 [89] TeV,
- Z -production data differential in rapidity from the ATLAS experiment at 7 [88] and 8 [90] TeV,
- off-peak (low- and high-mass) DY data from the ATLAS experiment at 8 TeV [90],
- preliminary Z -production data from the STAR experiment at 510 GeV.⁶

⁶We thank the STAR Collaboration for providing us with the data.

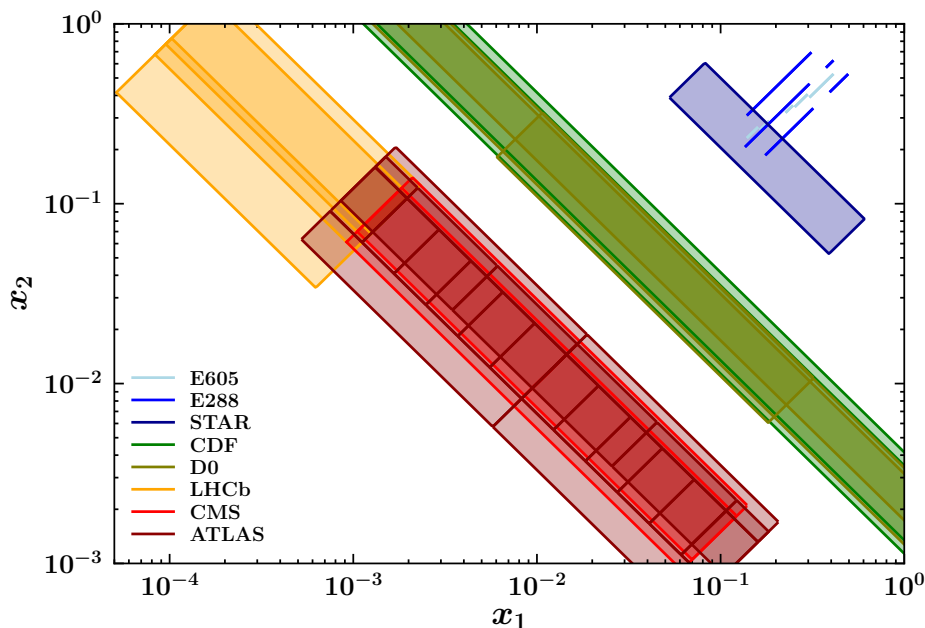


Figure 3. Kinematic coverage on the x_1 vs. x_2 plane of the dataset included in the present analysis.

Finally, we originally considered also measurements from the PHENIX experiment at the center-of-mass energy of 200 GeV [91]. However, due to the cut on q_T/Q discussed below, only two data points from this dataset would be included in the fit. Therefore, we decided to exclude it.

The breakdown of the entire dataset included in our analysis is reported in table 2. For visualisation purposes, in figure 3 we show the kinematic coverage of each datasets in the x_1 vs. x_2 plane, with $x_{1,2} = Qe^{\pm y}/\sqrt{s}$. The shaded areas are determined considering the corresponding ranges in Q and y , and the center-of-mass energy \sqrt{s} .⁷ As expected, the lower-energy experiments (E605, E288, and STAR) are placed in the large- x region ($x \gtrsim 0.1$). Particularly important are the new (preliminary) STAR measurements that cover a kinematic region that is scarcely populated. The Tevatron experiments, CDF and D0, cover a particularly wide kinematic region at intermediate values of x . These experiments (except D0 Run II with muons) provide data extrapolated over the full range in rapidity y , thus extending across the full available phase space. Finally, the LHC experiments (LHCb, CMS, and ATLAS) are placed at lower values of x . The LHCb datasets are in a region in which x_1 is particularly small and x_2 particularly large: this is due to the fact that the data is taken in the forward region, $2 < y < 4.5$. The ATLAS datasets are binned in rapidity and thus are expected to be particularly sensitive to the x dependence of the TMDs. Indeed, we will show below that the x dependence of TMDs is mostly constrained by these datasets.

Since our analysis is based on the TMD factorisation formula in eq. (2.10), only data at small q_T can possibly be described. Hence, we impose a cut to exclude measurements

⁷It should be kept in mind that figure 3 only provides an approximated view of the real coverage, strictly true only at tree level. The reason is that x_1 and x_2 are just the lower bounds of convolution integrals (see, e.g., eq. (2.17)). Therefore, the effective region of sensitivity actually extends between $x_{1,2}$ and 1.

Experiment	N_{dat}	Observable	\sqrt{s} [GeV]	Q [GeV]	y or x_F	Lepton cuts	Ref.
E605	50	$Ed^3\sigma/d^3q$	38.8	7–18	$x_F = 0.1$	-	[79]
E288 200 GeV	30	$Ed^3\sigma/d^3q$	19.4	4–9	$y = 0.40$	-	[80]
E288 300 GeV	39	$Ed^3\sigma/d^3q$	23.8	4–12	$y = 0.21$	-	[80]
E288 400 GeV	61	$Ed^3\sigma/d^3q$	27.4	5–14	$y = 0.03$	-	[80]
STAR 510	7	$d\sigma/dq_T$	510	73–114	$ y < 1$	$p_{T\ell} > 25$ GeV $ \eta_\ell < 1$	-
CDF Run I	25	$d\sigma/dq_T$	1800	66–116	Inclusive	-	[81]
CDF Run II	26	$d\sigma/dq_T$	1960	66–116	Inclusive	-	[82]
D0 Run I	12	$d\sigma/dq_T$	1800	75–105	Inclusive	-	[83]
D0 Run II	5	$(1/\sigma)d\sigma/dq_T$	1960	70–110	Inclusive	-	[84]
D0 Run II (μ)	3	$(1/\sigma)d\sigma/dq_T$	1960	65–115	$ y < 1.7$	$p_{T\ell} > 15$ GeV $ \eta_\ell < 1.7$	[85]
LHCb 7 TeV	7	$d\sigma/dq_T$	7000	60–120	$2 < y < 4.5$	$p_{T\ell} > 20$ GeV $2 < \eta_\ell < 4.5$	[86]
LHCb 8 TeV	7	$d\sigma/dq_T$	8000	60–120	$2 < y < 4.5$	$p_{T\ell} > 20$ GeV $2 < \eta_\ell < 4.5$	[87]
LHCb 13 TeV	7	$d\sigma/dq_T$	13000	60–120	$2 < y < 4.5$	$p_{T\ell} > 20$ GeV $2 < \eta_\ell < 4.5$	[92]
CMS 7 TeV	4	$(1/\sigma)d\sigma/dq_T$	7000	60–120	$ y < 2.1$	$p_{T\ell} > 20$ GeV $ \eta_\ell < 2.1$	[88]
CMS 8 TeV	4	$(1/\sigma)d\sigma/dq_T$	8000	60–120	$ y < 2.1$	$p_{T\ell} > 15$ GeV $ \eta_\ell < 2.1$	[89]
ATLAS 7 TeV	6 6 6	$(1/\sigma)d\sigma/dq_T$	7000	66–116	$ y < 1$ $1 < y < 2$ $2 < y < 2.4$	$p_{T\ell} > 20$ GeV $ \eta_\ell < 2.4$	[93]
ATLAS 8 TeV on-peak	6 6 6 6 6	$(1/\sigma)d\sigma/dq_T$	8000	66–116	$ y < 0.4$ $0.4 < y < 0.8$ $0.8 < y < 1.2$ $1.2 < y < 1.6$ $1.6 < y < 2$ $2 < y < 2.4$	$p_{T\ell} > 20$ GeV $ \eta_\ell < 2.4$	[90]
ATLAS 8 TeV off-peak	4 8	$(1/\sigma)d\sigma/dq_T$	8000	46–66 116–150	$ y < 2.4$	$p_{T\ell} > 20$ GeV $ \eta_\ell < 2.4$	[90]
Total	353	-	-	-	-	-	-

Table 2. Breakdown of the datasets included in this analysis. For each dataset, the table includes information on: the number of data points (N_{dat}) passing the nominal cut on q_T/Q , the observable delivered, the center of mass energy \sqrt{s} , the range(s) in invariant mass Q , the angular variable (either y or x_F), possible cuts on the single final-state leptons, and the public reference (when available). The total number of data points amounts to 353. Note that for E605 and E288 400 GeV we have excluded the bin in Q containing the Υ resonance ($Q \simeq 9.5$ GeV).

with large q_T by requiring $q_T/Q < 0.2$. Since the measurements are delivered in transverse-momentum bins $[q_{T,\min}: q_{T,\max}]$ integrated over some range in invariant mass $[Q_{\min}: Q_{\max}]$, the cut is conservatively imposed on the ratio $q_{T,\max}/Q_{\min}$. The second column in table 2 reports the number of data points (N_{dat}) for each dataset that pass this cut: the total number of points included in our analysis is 353.

An important feature of all the new datasets listed above is that the cross sections are given within a certain fiducial region. In particular, kinematic cuts on transverse momentum $p_{T\ell}$ and pseudo-rapidity η_ℓ of the final-state leptons are enforced. The values of the cuts are reported in the next-to-last column of table 2. Our predictions are corrected by means of the phase-space reduction factor \mathcal{P} introduced in eq. (2.10), which takes into account these cuts. Details concerning the calculation of \mathcal{P} are given in appendix C.

As evident from the ‘‘Observable’’ column of table 2, experimental cross sections are released in different forms. In addition, some of them are normalised to the total (fiducial) cross section while others are not. In our analysis, we expressed all the absolute cross sections in terms of the observable given in eq. (2.10) (details on the transformations between different observables can be found in ref. [21]). When necessary, the total cross section σ required to normalise the differential cross sections is computed using DYNNLO [94, 95] with the MMHT2014 collinear PDF sets [54], taking into account the selection cuts and consistently with the perturbative order of the differential cross section. More precisely, the total cross section is computed at LO for NLL accuracy, at NLO for NLL’ and NNLL, and at NNLO for NNLL’ and N³LL. The values of the total cross sections at different orders are reported in table 3. We stress that in this analysis no additional normalisations have been applied, with the consequence that both the shape and the normalisation of the experimental distributions have an impact on the fit.

Most of the considered experimental datasets are released with a set of *uncorrelated* and *correlated* uncertainties. As already pointed out in ref. [16], a proper treatment of the experimental uncertainties is crucial to achieve a reliable extraction of TMDs. In other words, the χ^2 , which quantifies the agreement between data and predictions and is minimised during the fit, has to be computed taking into account the nature of the various uncertainties. Particular care has to be taken with the (correlated) *normalisation* uncertainties. As is well known, an inappropriate description of normalisation uncertainties may lead to underestimate the predictions: that is the so-called D’Agostini bias [96, 97]. Different prescriptions have been devised to avoid this problem [98]: in this analysis we adopt the so-called iterative t_0 -prescription [99].

In the presence of correlated uncertainties, the χ^2 can be split as [98]

$$\chi^2 = \chi_D^2 + \chi_\lambda^2, \tag{3.1}$$

where χ_D^2 has an uncorrelated structure (diagonal) while χ_λ^2 is a penalty term related to the presence of correlations (see, e.g., appendix B of ref. [16]). For the computation of χ_D^2 , theoretical predictions are properly shifted to take into account the effect of the correlated uncertainties. In fact, shifted predictions are a better proxy for visual comparisons to experimental data. Therefore, in the following it is understood that all plots will display shifted predictions.

Experiment	LO [pb]	NLO [pb]	NNLO [pb]	
D0 Run II	170.332	242.077	253.573	
D0 Run II (μ)	100.765	119.002	124.675	
CMS 7 TeV	291.977	384.569	398.853	
CMS 8 TeV	340.132	456.337	473.411	
ATLAS 7 TeV	$ y < 1$	196.457	251.296	253.781
	$1 < y < 2$	135.511	181.267	181.466
	$2 < y < 2.4$	12.568	17.091	17.104
ATLAS 8 TeV	$ y < 0.4$	89.531	113.650	116.766
	$0.4 < y < 0.8$	89.120	112.853	115.738
	$0.8 < y < 1.2$	85.499	109.800	112.457
	on-peak $1.2 < y < 1.6$	69.018	91.884	95.187
	$1.6 < y < 2$	43.597	59.114	62.127
	$2 < y < 2.4$	14.398	19.574	20.937
	off-peak			
ATLAS 8 TeV $46 \text{ GeV} < Q < 66 \text{ GeV}$	15.199	14.449	14.368	
off-peak $116 \text{ GeV} < Q < 150 \text{ GeV}$	3.805	5.317	5.521	

Table 3. Total (fiducial) cross sections computed with DYNNLO [94, 95] using the central member of the MMHT2014 collinear PDF sets [54] and required for the computation of the normalised differential cross sections at the different perturbative orders.

A further important aspect is the use of collinear PDFs. In order to extract f_{NP} defined in eq. (2.36), it is necessary to assume a given set of collinear PDFs (MMHT2014 in our case). PDF uncertainties reflect the experimental uncertainty of the dataset used for their extraction. It is therefore natural to attribute an experimental nature to this uncertainty and include it in the calculation of the χ^2 . To do so, we computed the PDF errors as relative to the central value⁸ and included them in the experimental covariance matrix as uncorrelated uncertainties. The propagation of the resulting experimental uncertainty into the fitted TMDs is achieved through Monte Carlo sampling. Specifically, we generate N_{rep} ($\gtrsim 200$) replicas of the original dataset taking into account all the uncertainties and then perform a fit on each single replica. The resulting ensemble of distributions can be used to compute central values and uncertainties as averages and correlations, respectively.

A final remark concerns the integration over the final-state phase space. The basic quantity to be compared to data is

$$\frac{d\sigma}{dq_T} = \frac{1}{q_{T,\text{max}} - q_{T,\text{min}}} \int_{y_{\text{min}}}^{y_{\text{max}}} dy \int_{Q_{\text{min}}}^{Q_{\text{max}}} dQ \int_{q_{T,\text{min}}}^{q_{T,\text{max}}} dq_T \left[\frac{d\sigma}{dQ dy dq_T} \right], \quad (3.2)$$

where the ranges $[y_{\text{min}}: y_{\text{max}}]$, $[Q_{\text{min}}: Q_{\text{max}}]$, and $[q_{T,\text{min}}: q_{T,\text{max}}]$ define the phase-space integration region and the integrand is given in eq. (2.10). In order to speed up the

⁸The advantage of computing relative uncertainties is that of minimising the dependence on the non-perturbative function f_{NP} assumed for the computation of both the central PDF set and the error members. We also notice that the calculation of such uncertainties does include the PDF uncertainty on the total cross sections when normalised distributions are considered.

numerical computation of the theoretical predictions, the integration over the bins in q_T and Q is often performed approximating the q_T -bin integral with its central value and using the narrow-width approximation for the integral over Q around the Z peak. We stress that in this analysis the integrals in eq. (3.2) are computed *exactly*. While the integrals over y and Q do need to be computed numerically, the integral over q_T can be performed (semi)analytically exploiting a property of the Bessel functions J_n (see appendix B). This greatly reduces the amount of numerical computations.

4 Results

In this section, we present the results of our extraction of unpolarised TMDs from a comprehensive set of DY data (see section 3). In section 4.1, we present the quality of the fit at N³LL, the best accuracy we can presently reach. In section 4.2 we discuss the TMDs extracted from the nominal fit. In section 4.3, we discuss the convergence of the perturbative corrections. In section 4.4, we focus on the x dependence of the TMDs and we argue that it is mostly constrained by the y -differential ATLAS cross sections. Finally, in section 4.5, we assess the range of validity of TMD factorisation by considering the fit quality as a function of the cut on q_T/Q .

4.1 Fit quality

In this section, we discuss the quality of the reference fit at N³LL with cut $q_T/Q < 0.2$. In order to quantify this quality, the χ^2 s are evaluated using the mean of the TMDs extracted from the Monte Carlo replicas of the data. Denoting the Monte Carlo ensemble of TMDs with $\{\hat{f}_1^{q,[k]}\}$, $k = 1, \dots, N_{\text{rep}}$ (N_{rep} being the number of replicas), the *mean* is defined as

$$\hat{f}_1^q(x, b_T; \mu, \zeta) = \frac{1}{N_{\text{rep}}} \sum_{k=1}^{N_{\text{rep}}} \hat{f}_1^{q,[k]}(x, b_T; \mu, \zeta). \quad (4.1)$$

The mean value provides a *democratic* representative of the ensemble. Other choices are possible, such as the median or the mode of the ensemble. In fact, only the full ensemble of replicas carries the full statistical information. However, the reason for using eq. (4.1) is that quantifying the goodness of our fit becomes easier, as it will be clear in the following.

Table 4 reports the breakdown of the χ^2 s normalised to the number of data points, N_{dat} , for each dataset. The uncorrelated (χ_D^2) and the correlated (χ_λ^2) contributions to the total χ^2 (see eq. (3.1)) are also reported. The global χ^2 is shown at the bottom of the table.

The value of the global χ^2 is very close to one (1.02), indicating that the fit is able to describe measurements over a wide energy range, from the low-energy fixed-target datasets to the LHC ones. It is important to stress that a substantial contribution to the global χ^2 is given by the correlated penalty term, $\chi_\lambda^2/N_{\text{dat}} = 0.14$. This highlights the importance of a correct treatment of the correlated uncertainties. More specifically, the systematic shifts induced by correlations are often large, indicating that the fit does need to adjust the predictions within the experimentally correlated ranges.

Concerning the single experiments, we observe that the low-energy data (E605, E288, and STAR) have generally lower χ^2 s than the Tevatron (CDF and D0) and LHC (LHCb,

Experiment		χ_D^2/N_{dat}	$\chi_\lambda^2/N_{\text{dat}}$	χ^2/N_{dat}
E605	7 GeV < Q < 8 GeV	0.419	0.068	0.487
	8 GeV < Q < 9 GeV	0.995	0.034	1.029
	10.5 GeV < Q < 11.5 GeV	0.191	0.137	0.328
	11.5 GeV < Q < 13.5 GeV	0.491	0.284	0.775
	13.5 GeV < Q < 18 GeV	0.491	0.385	0.877
E288 200 GeV	4 GeV < Q < 5 GeV	0.213	0.649	0.862
	5 GeV < Q < 6 GeV	0.673	0.292	0.965
	6 GeV < Q < 7 GeV	0.133	0.141	0.275
	7 GeV < Q < 8 GeV	0.254	0.014	0.268
	8 GeV < Q < 9 GeV	0.652	0.024	0.676
E288 300 GeV	4 GeV < Q < 5 GeV	0.231	0.555	0.785
	5 GeV < Q < 6 GeV	0.502	0.204	0.706
	6 GeV < Q < 7 GeV	0.315	0.063	0.378
	7 GeV < Q < 8 GeV	0.056	0.030	0.086
	8 GeV < Q < 9 GeV	0.530	0.017	0.547
	11 GeV < Q < 12 GeV	1.047	0.167	1.215
E288 400 GeV	5 GeV < Q < 6 GeV	0.312	0.065	0.377
	6 GeV < Q < 7 GeV	0.100	0.005	0.105
	7 GeV < Q < 8 GeV	0.018	0.011	0.029
	8 GeV < Q < 9 GeV	0.437	0.039	0.477
	11 GeV < Q < 12 GeV	0.637	0.036	0.673
	12 GeV < Q < 13 GeV	0.788	0.028	0.816
	13 GeV < Q < 14 GeV	1.064	0.044	1.107
STAR		0.782	0.054	0.836
CDF Run I		0.480	0.058	0.538
CDF Run II		0.959	0.001	0.959
D0 Run I		0.711	0.043	0.753
D0 Run II		1.325	0.612	1.937
D0 Run II (μ)		3.196	0.023	3.218
LHCb 7 TeV		1.069	0.194	1.263
LHCb 8 TeV		0.460	0.075	0.535
LHCb 13 TeV		0.735	0.020	0.755
CMS 7 TeV		2.131	0.000	2.131
CMS 8 TeV		1.405	0.007	1.412
ATLAS 7 TeV	0 < $ y $ < 1	2.581	0.028	2.609
	1 < $ y $ < 2	4.333	1.032	5.365
	2 < $ y $ < 2.4	3.561	0.378	3.939
ATLAS 8 TeV on-peak	0 < $ y $ < 0.4	1.924	0.337	2.262
	0.4 < $ y $ < 0.8	2.342	0.247	2.590
	0.8 < $ y $ < 1.2	0.917	0.061	0.978
	1.2 < $ y $ < 1.6	0.912	0.095	1.006
	1.6 < $ y $ < 2	0.721	0.092	0.814
	2 < $ y $ < 2.4	0.932	0.348	1.280
ATLAS 8 TeV off-peak	46 GeV < Q < 66 GeV	2.138	0.745	2.883
	116 GeV < Q < 150 GeV	0.501	0.003	0.504
Global		0.88	0.14	1.02

Table 4. The χ^2/N_{dat} using the mean replica in eq. (4.1). N_{dat} in each case is listed in table 2. The uncorrelated (χ_D^2) and correlated (χ_λ^2) contributions and their sum χ^2 are shown (see eq. (3.1)).

CMS, and ATLAS) high-energy data. This is mostly due to the fact that the experimental uncertainties of the former are typically larger than the latter. In particular, the low-energy data are affected by large normalisation (correlated) uncertainties. Consequently, the relative importance of the correlated contribution χ_λ^2 to the total χ^2 is generally larger for the low-energy datasets than for the high-energy ones.

It is interesting to comment on the quality of the fit to the new datasets from RHIC and the LHC that were not included in the analysis of ref. [21] (see section 3). The preliminary measurements from STAR have a χ^2 equal to 0.836. This is particularly encouraging because, as clear from figure 3, this dataset covers a scarcely populated kinematic region and shows no tension with other data. Also the LHC datasets extend the kinematic coverage of the DY data considered in ref. [21]. These measurements are particularly precise and thus very effective in constraining TMDs. We observe that the LHCb datasets are very nicely described with χ^2 s that never exceed 1.3. The CMS data, despite having slightly larger χ^2 , are also well described. The two CMS datasets provide only eight points in total and thus their impact on the fit is modest. The ATLAS datasets, amongst the LHC ones, are by far the most abundant. We observe that the ATLAS 8 TeV datasets are well described, except for the first two low-rapidity bins. The 7 TeV ones present larger values of χ^2 , above 2. Given the extremely high precision of these datasets, even small effects (e.g., power corrections) could give a significant contribution to χ^2 in these conditions. We consider it already a success to obtain a value of χ^2 for these datasets that does not affect too much the global χ^2 . We note that a key feature of these datasets (except the off-peak ones) is that they are differential in the vector-boson rapidity y . As we will see in section 4.4, the x dependence of f_{NP} plays a crucial role in improving the χ^2 .

In order to provide a visual assessment of the fit quality, figure 4 displays the data/theory comparison for a representative selection of datasets. We remind the reader that in each plot theoretical predictions are appropriately shifted to account for correlated uncertainties [16], while the experimental error bars are given by the sum in quadrature of the uncorrelated uncertainties. The upper panel of each plot shows the absolute q_T distribution, while the lower panel shows the ratio to data. The plots in the upper row of figure 4 refer to one invariant-mass bin of E605 and CDF Run II already considered in ref. [21]. The remaining plots refer to some of the new datasets, namely STAR, LHCb 8 TeV, ATLAS 8 TeV on-peak at $1.6 < |y| < 2$, and ATLAS 8 TeV off-peak at $116 \text{ GeV} < Q < 150 \text{ GeV}$. As expected, there is a very good agreement between data and theory, for both the old and the new datasets. Finally, it is interesting to observe that the uncertainties of the upper and middle rows of figure 4 are larger than those in the two lower rows. This is due to the fact that the ATLAS distributions are normalised to the total cross section leading to a cancellation of some uncertainties, such as those due to luminosity and collinear PDFs.

4.2 TMD distributions

We discuss now the TMD distributions extracted from our reference N^3LL fit. We stress once again that only the combination in the r.h.s. of eq. (2.36) is meaningful.

In order to assess the sensitivity of the experimental dataset to f_{NP} , it is interesting to look at the values of the free parameters obtained from the fit. In table 5 the average of each

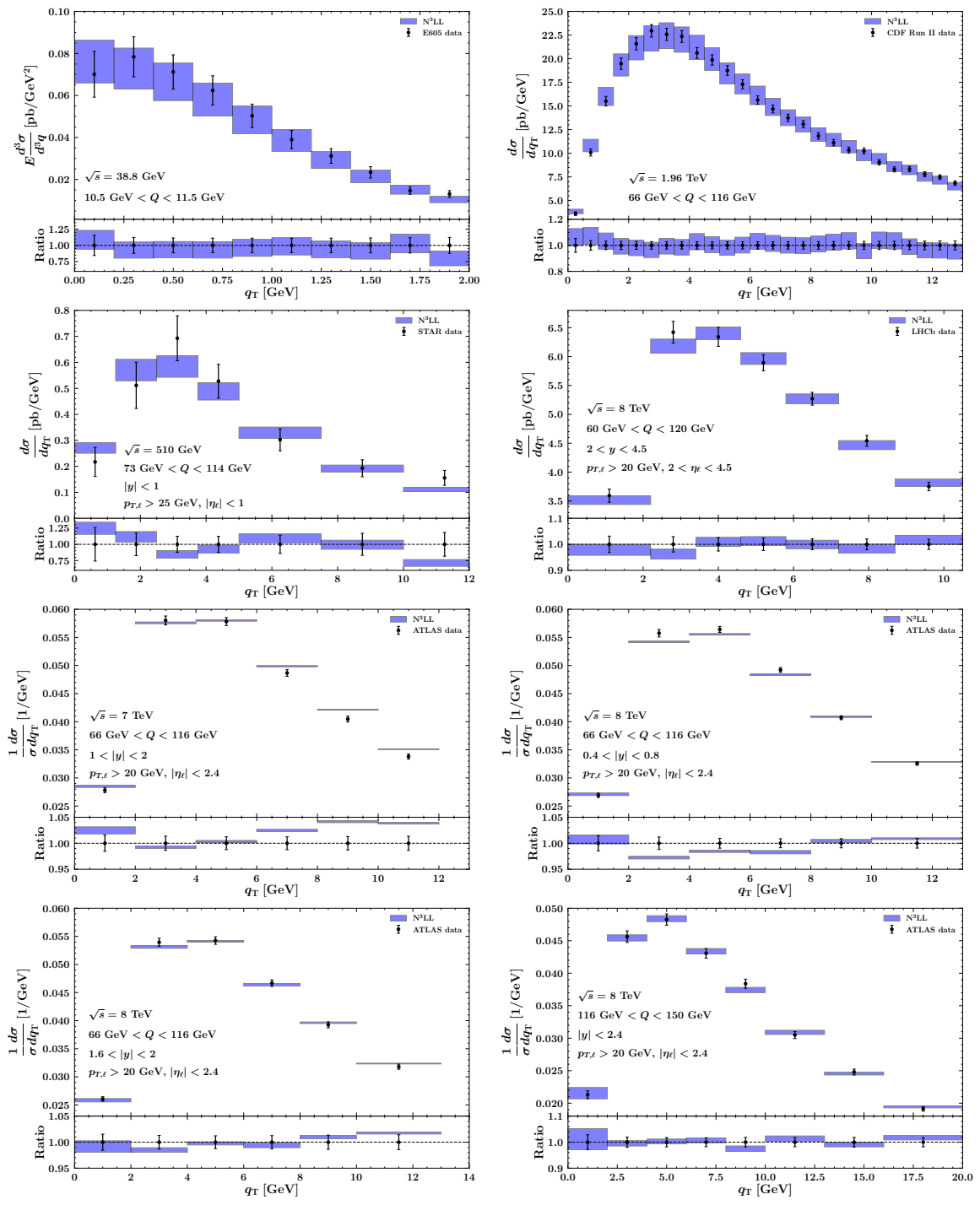


Figure 4. Comparison between experimental data and theoretical predictions obtained at N^3LL accuracy for a representative subset of the datasets included in this analysis. The upper panel of each plot displays the absolute q_T distributions, while the lower panel displays the same distributions normalised to the experimental central values. The blue bands represent the $1\text{-}\sigma$ uncertainty of the theoretical predictions.

Parameter	Value
g_2	0.036 ± 0.009
N_1	0.625 ± 0.282
α	0.205 ± 0.010
σ	0.370 ± 0.063
λ	0.580 ± 0.092
N_{1B}	0.044 ± 0.012
α_B	0.069 ± 0.009
σ_B	0.356 ± 0.075
g_{2B}	0.012 ± 0.003

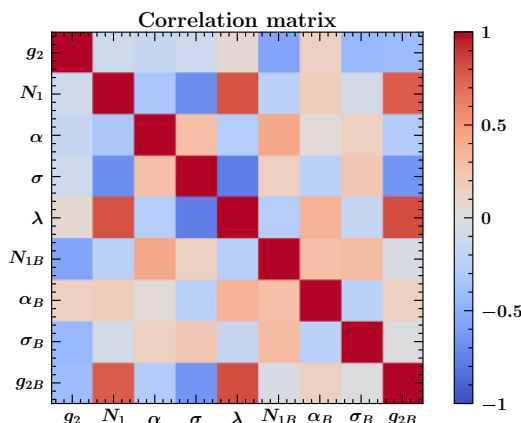


Table 5. Average and standard deviation over the Monte Carlo replicas of the free parameters fitted to the data and graphical representation of the correlation matrix.

parameter over the Monte Carlo replicas, along with the respective standard deviation, is reported. All parameters are well constrained.⁹ It is interesting to observe that the parameter λ , that measures the relative weight of Gaussian and q -Gaussian in eq. (2.39), is close to 0.5 indicating that these contributions weigh approximately the same. Concerning the values of the parameters g_2 and g_{2B} associated to the non-perturbative contribution to TMD evolution, we find that the coefficient g_{2B} of the quartic term is small but significantly different from zero. This seems to suggest that higher-power corrections to the commonly assumed quadratic term g_2 may be required by the data.

Further insight concerning the appropriateness of the functional form in eqs. (2.39)–(2.40) can be gathered by looking at the statistical correlations between parameters. In the right panel of table 5, we show a graphical representation of the correlation matrix of the fitted parameters. The first observation is that (off-diagonal) correlations are generally not very large. There is however one exception, i.e. the parameters σ and λ seem to be strongly anti-correlated. This may indicate that the interplay between q -Gaussian and Gaussian may be significantly x dependent. We leave a deeper study of this feature to a future publication.

To conclude this section, in figure 5 we show the down-quark TMD at $\mu = \sqrt{\bar{\zeta}} = Q = 2$ GeV (left plot) and 10 GeV (right plot) as a function of the partonic transverse momentum k_\perp for $x = 0.001, 0.1, 0.3$. The $1-\sigma$ uncertainty bands are also shown. As expected, TMDs are suppressed as k_\perp grows and the suppression becomes relatively stronger as Q increases.

4.3 Perturbative convergence

In the previous section we discussed the quality of our fit at N³LL, which is the best accuracy presently available. In this section we show how the inclusion of perturbative corrections is crucial to achieve a better description of the experimental data. To this end, we performed fits at NLL', NNLL, and NNLL' (see section 2.4), and compared them to the

⁹We stress that the parameters reported in table 5 are not meant to be used in the parameterisation in eqs. (2.39)–(2.40) as they are not a direct result of any of our fits.

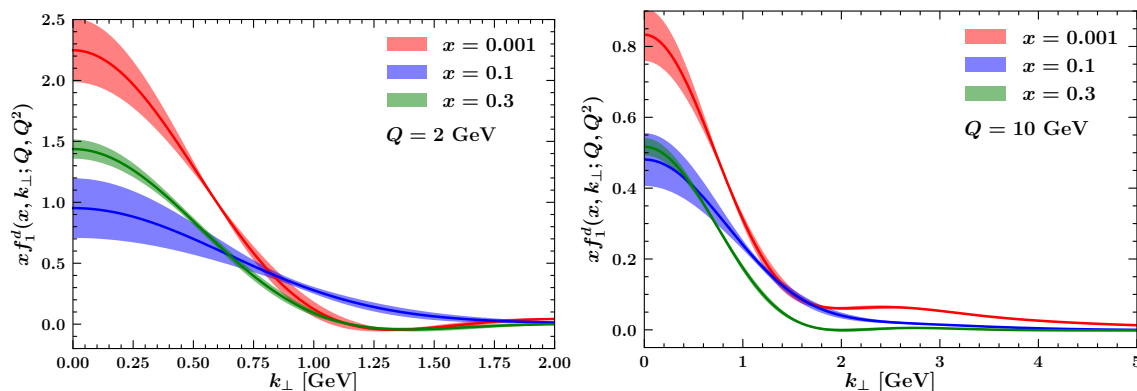


Figure 5. The TMD of the down quark at $\mu = \sqrt{\zeta} = Q = 2$ GeV (left plot) and 10 GeV (right plot) as a function of the partonic transverse momentum k_{\perp} for three different values of x . The bands give the 1- σ uncertainty.

	NLL'	NNLL	NNLL'	N ³ LL
Global χ^2	1126	571	379	360

Table 6. Values of the global χ^2 of the fits at NLL', NNLL, NNLL', and N³LL accuracy.

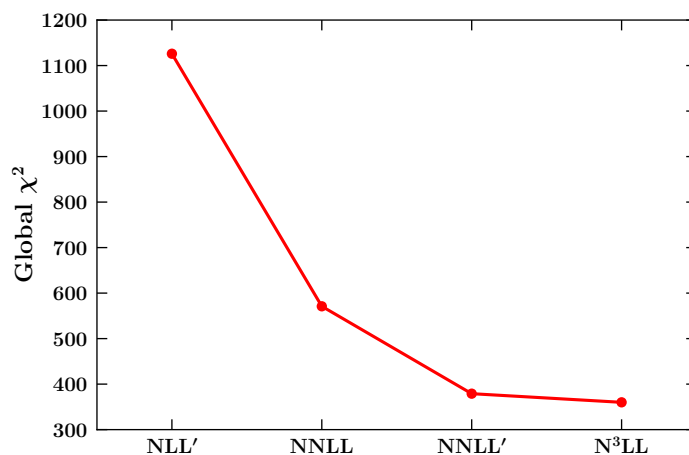


Figure 6. Graphical representation of table 6.

N³LL fit. We did not consider LL and NLL accuracies because in both cases the description of the data is very poor ($\chi^2 \gtrsim 20$).

Table 6 reports the values of the global χ^2 for each of the four accuracies considered. In order to appreciate the significance of the differences,¹⁰ we have reported the absolute values of the χ^2 without dividing by the number of data points N_{dat} . Figure 6 shows a graphical representation of table 6. The global quality of the fit improves significantly as the perturbative accuracy increases. In addition, figure 6 shows that the convergence rate decreases when going to larger perturbative orders. On the one hand, we conclude that it

¹⁰Note that a difference of n units at the level of the global χ^2 roughly means a separation of around \sqrt{n} standard deviations.

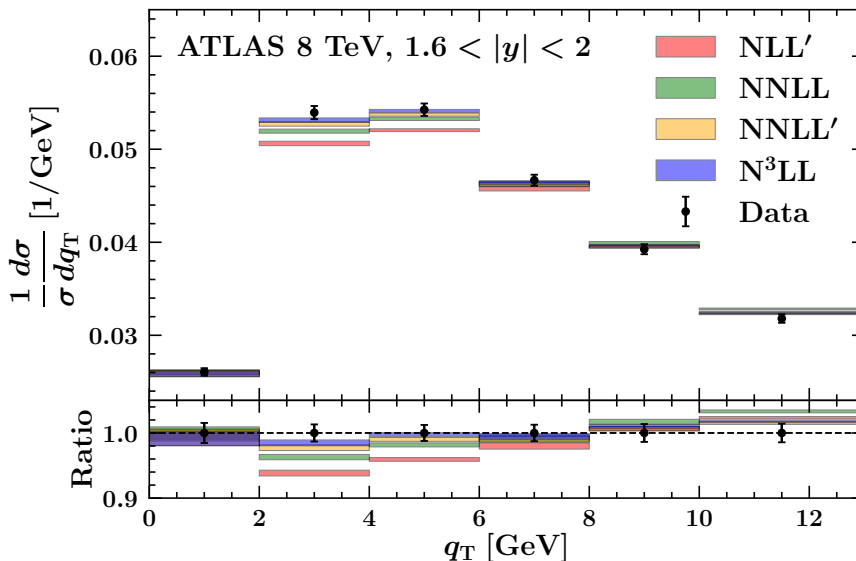


Figure 7. Comparison between experimental data for the ATLAS 8 TeV measurements in the bin $66 \text{ GeV} < Q < 116 \text{ GeV}$ and $1.6 < |y| < 2$ and the theoretical predictions obtained from the fits to all perturbative orders considered in this analysis, i.e. NLL', NNLL, NNLL', and N³LL (see section 2.4). The layout of the plot is the same as in figure 4.

is necessary to include higher perturbative corrections to obtain a good description of the data and that N³LL corrections are still significant. On the other hand, it appears that the perturbative series is nicely converging and N³LL accuracy seems appropriate within the current experimental uncertainties.

In order to quantify the numerical impact of higher-order corrections, in figure 7 we compare the predictions for all the available perturbative orders to the ATLAS 8 TeV data in the bin $66 \text{ GeV} < Q < 116 \text{ GeV}$ and $1.6 < |y| < 2$. This plot shows how the inclusion of higher-order corrections improves the shape of the predictions, particularly around the peak region.

4.4 Reduced dataset and x dependence

The non-perturbative function f_{NP} , eq. (2.36), accounts for the large- b_T behaviour of TMDs. It is in general a function of b_T , ζ , and x . While the asymptotic dependence on b_T is driven by first-principle considerations (see section 2.5) and the evolution with ζ is determined by the Collins-Soper equation (2.11), the dependence on x is totally unknown. Moreover, a direct access to the x dependence is particularly difficult to achieve because it requires cross-section data finely binned in rapidity y . In the dataset considered here, only the ATLAS experiment delivers data differential in rapidity. Therefore, one would expect that these datasets provide most of the sensitivity to the x dependence of TMDs.

In order to test this conjecture, we employed a particularly simple x -independent parameterisation of the non-perturbative function:

$$f_{\text{NP}}^{\text{DWS}}(b_T, \zeta) = \exp \left[-\frac{1}{2} \left(g_1 + g_2 \ln \left(\frac{\zeta}{2Q_0^2} \right) \right) b_T^2 \right], \quad (4.2)$$

	Full dataset	No y -differential data
Global χ^2/N_{dat}	1.339	0.895
g_1	0.304	0.207
g_2	0.028	0.093

Table 7. The values of the global χ^2 normalised to the number of data points N_{dat} from the fit to the full dataset and to a reduced dataset without the y -differential ATLAS datasets, both using the parameterisation in eq. (4.2). For completeness, we also report the best-fit values of the parameters g_1 and g_2 .

with two free parameters, g_1 and g_2 , and $Q_0^2 = 1.6 \text{ GeV}^2$ (inspired by the pioneering work of Davies, Webber, and Stirling. [4]). Using eq. (4.2) we first performed a fit at N³LL to the full dataset. Then we excluded the ATLAS datasets differential in rapidity (but we kept the off-peak ATLAS 8 TeV datasets because inclusive in rapidity). The resulting χ^2 s normalised to the number of data points are reported in table 7. For completeness, we also show the best-fit values of the parameters g_1 and g_2 .

Firstly, the χ^2 of the fit to the full dataset using eq. (4.2) (1.339) is significantly larger than that obtained using the parameterisation in eqs. (2.39)–(2.40) (1.020). This suggests that an x -dependent f_{NP} is required to obtain a good description of the data. Secondly, the χ^2 of the fit without the y -differential ATLAS data comes out to be particularly low (0.895). We conclude that at N³LL accuracy the x dependence of the TMDs extracted from the currently available DY data is mostly constrained by the ATLAS data differential in the boson rapidity y . We note however that the agreement with the very precise ATLAS data may be influenced also by other small corrections (e.g. power corrections).

4.5 Dependence on the cut on q_T/Q

As discussed in section 2, our analysis is based on TMD factorisation whose validity is restricted to the region $q_T \ll Q$. As a consequence, we consider only measurements that respect this constraint. More precisely, we require that the maximum value of the ratio q_T/Q for a point to be included in the fit be 0.2 (see section 3). Despite this particular value seems to be generally recognised in the literature (see, e.g., ref. [15]), it is interesting to study how the global description of the dataset changes by varying this cut. This will help us assess more quantitatively the validity range of TMD factorisation.

Figure 8 displays the behaviour of the global χ^2/N_{data} for the N³LL fit as a function of the q_T/Q cut ranging between 0.1 and 0.28 in steps of 0.02. As expected, the quality of the fit tends to degrade as the cut on q_T/Q increases. Of course, it is impossible to draw a line between validity and non-validity regions. However, this study gives a quantitative justification for choosing the value 0.2 for the q_T/Q cut.

5 Conclusions

In this paper we presented an extraction of TMDs from Drell-Yan data accurate up to N³LL. The dataset used in this analysis includes low-energy data from FNAL (E605 and

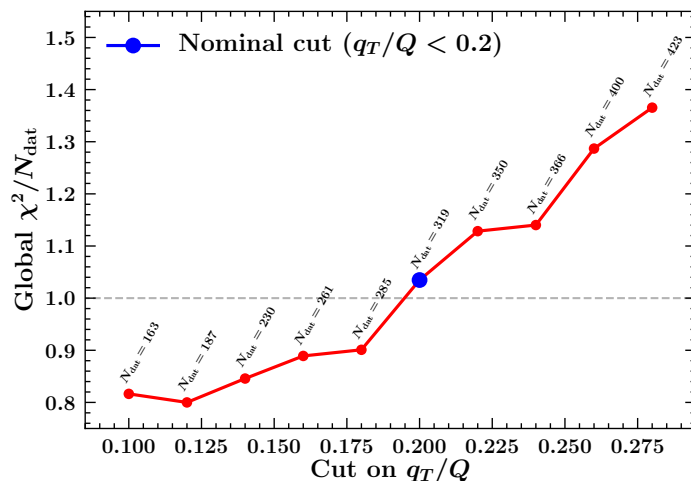


Figure 8. The global χ^2/N_{dat} as a function of the cut on q_T/Q . The blue point corresponds to the reference cut used in this analysis.

E288) and RHIC (STAR) and high-energy data from Tevatron (CDF and D0) and the LHC (LHCb, CMS, and ATLAS), for a total of 353 data points.

The fit was performed with a proper treatment of the experimental uncertainties, which were propagated into the fitted TMD distributions by means of the Monte Carlo sampling method. This allowed us to obtain a very good description of the entire dataset ($\chi^2/N_{\text{dat}} = 1.02$) without the need of introducing *ad hoc* normalisations. A more detailed analysis of the fit quality shows that both low- and high-energy datasets are separately well described. This is a remarkable achievement given the very high precision of the LHC datasets, especially those from ATLAS.

A particularly interesting aspect of our analysis concerns the QCD convergence of the perturbative series. We performed fits at NLL', NNLL, NNLL', and N³LL accuracy and showed that the fit quality improves significantly going from NLL' to N³LL. The difference between the highest orders, i.e. NNLL' and N³LL, is moderate but still significant. This shows at the same time that the perturbative series is converging, but also that N³LL corrections are relevant in relation to the current experimental uncertainties.

We parameterised the non-perturbative contributions by adopting a reasonably flexible functional form: all nine free parameters turned out to be well constrained, with moderate correlations amongst them. An important feature of our parameterisation of the non-perturbative contribution f_{NP} is its explicit x dependence. We proved that the x -dependent part of f_{NP} is mostly constrained by the rapidity-dependent on-peak data at 7 and 8 TeV from ATLAS. While on the one hand, this was to be expected because the x dependence is strictly connected with the rapidity y , on the other hand it also demonstrates that most of the datasets are not sensitive to the x dependence of TMDs.

Finally, we studied the validity range of TMD factorisation in Drell-Yan by varying the cut on q_T/Q . In line with the literature, we found that the region $q_T \lesssim 0.2 Q$ is appropriate when working within the TMD factorisation framework.

In this paper we set the foundation for a number of future studies. In the first place, we plan to extend the fitted dataset by including the abundant and precise semi-inclusive DIS data from HERMES [61] and COMPASS [62, 100], as well as future data from Jefferson Lab at 12 GeV [101]. On top of providing access to TMD fragmentation functions, we expect that the inclusion of semi-inclusive DIS data will have an impact on the determination of the x dependence of TMD PDFs and will make it possible to determine the flavour dependence of the non-perturbative function f_{NP} . We remark that a better knowledge of TMDs will be important not only to obtain a deeper knowledge of hadron structure and QCD, but also for precision studies in high-energy processes involving hadrons, for instance for the determination of critical Standard Model parameters such as the W mass [25, 63].

In the future, the Electron-Ion Collider will provide an unprecedented opportunity to make progress in the determination of TMDs [102, 103]. Nevertheless, we are convinced that the era of precision physics with TMDs has already started and it will be beneficial also for studies at higher energies in the perturbative domain of QCD.

Acknowledgments

We thank P.F. Monni for discussions concerning the different logarithmic orderings, and H. Avakyan for discussions on the functional forms for our parametrisation. This work is supported by the European Research Council (ERC) under the European Union’s Horizon 2020 research and innovation program (grant agreement No. 647981, 3DSPIN).

A Numerics and delivery

In this appendix we give a brief general overview of the numerical implementation of the analysis discussed above. The code used is publicly available at

<https://github.com/vbertone/NangaParbat>

where a more detailed documentation can be found along with a collection of results. The code uses APFEL++ [104, 105] as an engine for the computation of the theoretical predictions. In order to speed up the fit on the non-perturbative function f_{NP} , eq. (2.36), we use interpolation techniques inspired by those heavily used for collinear-factorisation predictions [106–108]. Schematically, we reduce the computation of the cross section in eq. (3.2) for a given kinematic bin to the weighted sum

$$\frac{d\sigma}{dq_T} \simeq \sum_{n,\alpha,\tau} W_{n\alpha\tau} f_{\text{NP}}(x_1^{(\alpha,\tau)}, b_T^{(n)}, \zeta^{(\tau)}) f_{\text{NP}}(x_2^{(\alpha,\tau)}, b_T^{(n)}, \zeta^{(\tau)}), \quad (\text{A.1})$$

where the discrete variables $x_{1,2}^{(\alpha,\tau)}$, $b_T^{(n)}$, and $\zeta^{(\tau)}$ run over appropriately defined grids. The computationally expensive part of the calculation is isolated into the weights $W_{n\alpha\tau}$ that are precomputed and stored. This procedure makes the computation of predictions very fast and thus suitable for a fit that requires a large number of iterations.

In order to fit the function f_{NP} to data, we used two independent codes: `Minuit2` [109] as implemented in `ROOT`, and `ceres-solver` [110]. While the first (`Minuit`) is routinely used

for this kind of tasks since many years, the second (`ceres-solver`) is relatively new and typically used for more complex problems such as image recognition, 3D modeling, etc.. Recently, the `xFitter` Collaboration [111] has used `ceres-solver` for fitting collinear PDFs [112], showing that this tool is suitable also for this kind of tasks. Having two independent codes within the same framework turned out to be particularly useful to cross check our results.

All the datasets included in this analysis, except the preliminary STAR data, have been taken from the public HEPData repository [113] in YAML format and slightly adapted to fit our needs.

Finally, we mention that the TMDs sets determined in this analysis will be made publicly available also through the `TMDplotter` interface [114].

B Integrating over q_T

Experimental measurements of differential distributions are usually delivered as integrated over finite regions of the final-state kinematic phase space (see eq. (3.2)). As a consequence, in order to compare theoretical predictions to data, it is necessary to carry out these integrations. These nested integrals, if evaluated numerically, represent a heavy task that makes an extraction of TMDs from Drell-Yan data computationally very intensive and thus slow. While the integrals over Q and y do need to be computed numerically, the integration in q_T can be carried out analytically which substantially reduces the numerical load. To do so, we exploit the following property of the Bessel functions

$$\frac{d}{dx} [x^n J_n(x)] = x^n J_{n-1}(x), \quad (\text{B.1})$$

that leads to

$$\int dx x J_0(x) = x J_1(x) \quad \Rightarrow \quad \int_{x_1}^{x_2} dx x J_0(x) = x_2 J_1(x_2) - x_1 J_1(x_1). \quad (\text{B.2})$$

Neglecting for the moment the dependence on q_T of the phase-space reduction factor \mathcal{P} (which is strictly correct for inclusive observables in the final-state leptons), the differential cross section in eq. (2.10) has the following structure

$$\frac{d\sigma}{dQdydq_T} = \int_0^\infty db_T S(b_T) q_T J_0(b_T q_T) \quad (\text{B.3})$$

where S is a function that depends on b_T (and on the other kinematic variables) but not on q_T . Using eq. (B.2), one finds

$$\begin{aligned} \int_{q_{T,\min}}^{q_{T,\max}} dq_T \left[\frac{d\sigma}{dQdydq_T} \right] &= \int_0^\infty db_T S(b_T) \int_{q_{T,\min}}^{q_{T,\max}} dq_T q_T J_0(b_T q_T) \\ &= \int_0^\infty db_T \frac{S(b_T)}{b_T} [q_{T,\max} J_1(b_T q_{T,\max}) - q_{T,\min} J_1(b_T q_{T,\min})]. \end{aligned} \quad (\text{B.4})$$

In conclusion, the quantity

$$K(q_T) \equiv \int_0^\infty db_T \frac{S(b_T)}{b_T} q_T J_1(b_T q_T), \quad (\text{B.5})$$

is the indefinite integral over q_T (the primitive function) of the cross section in eq. (2.10). Analogously to the unintegrated cross section, K can be computed numerically by performing a Bessel transform of degree one rather than degree zero. Therefore, the integral over a q_T bin can be evaluated by taking the difference of K computed at the bin bounds:

$$\int_{q_{T,\min}}^{q_{T,\max}} dq_T \left[\frac{d\sigma}{dQdydq_T} \right] = K(q_{T,\max}) - K(q_{T,\min}), \quad (\text{B.6})$$

which is enormously more convenient than computing the integral numerically.

B.1 Kinematic cuts

In the presence of kinematic cuts, such as those on the final-state leptons, the analytic integration over q_T discussed above cannot be directly performed. The reason is that the implementation of these cuts effectively introduces the q_T -dependent function \mathcal{P} in the integral

$$\frac{d\sigma}{dQdydq_T} = \int_0^\infty db_T S(b_T) \mathcal{P}(q_T) q_T J_0(b_T q_T), \quad (\text{B.7})$$

that prevents the direct use of eq. (B.2). Fortunately, \mathcal{P} is a slowly-varying function of q_T over the typical bin size. This allows one to approximate the integral over the bins in q_T as

$$\begin{aligned} \int_{q_{T,\min}}^{q_{T,\max}} dq_T q_T J_0(b_T q_T) \mathcal{P}(q_T) &\simeq \mathcal{P}\left(\frac{q_{T,\max} + q_{T,\min}}{2}\right) \int_{q_{T,\min}}^{q_{T,\max}} dq_T q_T J_0(b_T q_T) \\ &= \mathcal{P}\left(\frac{q_{T,\max} + q_{T,\min}}{2}\right) \frac{1}{b_T} [q_{T,\max} J_1(b_T q_{T,\max}) - q_{T,\min} J_1(b_T q_{T,\min})]. \end{aligned} \quad (\text{B.8})$$

Unfortunately, this structure is inconvenient because it mixes different bin bounds and prevents a recursive computation. However, it is possible to go further and, assuming that the bin width is small enough, we expand \mathcal{P} in the following two equivalent ways

$$\mathcal{P}\left(\frac{q_{T,\max} + q_{T,\min}}{2}\right) = \begin{cases} \mathcal{P}(q_{T,\min} + \Delta q_T) \simeq \mathcal{P}(q_{T,\min}) + \mathcal{P}'(q_{T,\min}) \Delta q_T \\ \mathcal{P}(q_{T,\max} - \Delta q_T) \simeq \mathcal{P}(q_{T,\max}) - \mathcal{P}'(q_{T,\max}) \Delta q_T \end{cases}, \quad (\text{B.9})$$

with

$$\Delta q_T = \frac{q_{T,\max} - q_{T,\min}}{2}. \quad (\text{B.10})$$

Plugging the expansions above into eq. (B.8), one finds

$$\begin{aligned} b_T \int_{q_{T,\min}}^{q_{T,\max}} dq_T q_T J_0(b_T q_T) \mathcal{P}(q_T) &\simeq q_{T,\max} J_1(b_T q_{T,\max}) [\mathcal{P}(q_{T,\max}) - \mathcal{P}'(q_{T,\max}) \Delta q_T] \\ &\quad - q_{T,\min} J_1(b_T q_{T,\min}) [\mathcal{P}(q_{T,\min}) + \mathcal{P}'(q_{T,\min}) \Delta q_T]. \end{aligned} \quad (\text{B.11})$$

The advantage of this formula as compared to eq. (B.8) is that each of the terms in the r.h.s. depends on one single bin bound in q_T rather than on a combination of two consecutive bounds. This allows for a recursive computation of predictions in neighbouring bins in q_T .

C Cuts on the final-state leptons

In this section, we derive the explicit expression of the phase-space reduction factor \mathcal{P} introduced in section 2. This factor is defined as¹¹

$$\mathcal{P}(q) = \frac{\int_{\text{fid. reg.}} d^4 p_1 d^4 p_2 \delta(p_1^2) \delta(p_2^2) \theta(p_{1,0}) \theta(p_{2,0}) \delta^{(4)}(p_1 + p_2 - q) L_{\perp}(p_1, p_2)}{\int d^4 p_1 d^4 p_2 \delta(p_1^2) \delta(p_2^2) \theta(p_{1,0}) \theta(p_{2,0}) \delta^{(4)}(p_1 + p_2 - q) L_{\perp}(p_1, p_2)}, \quad (\text{C.1})$$

where p_1 and p_2 are the four-momenta of the outgoing leptons. The integral in the numerator extends over the fiducial region defined by the cuts on the final-state leptons. The quantity L_{\perp} is defined as

$$L_{\perp} = g_{\perp}^{\mu\nu} L_{\mu\nu}, \quad (\text{C.2})$$

where $L_{\mu\nu}$ is the (parity-conserving part of the) *leptonic tensor* that, assuming massless leptons, reads

$$L^{\mu\nu} = 4(p_1^{\mu} p_2^{\nu} + p_2^{\mu} p_1^{\nu} - g^{\mu\nu} p_1 p_2), \quad (\text{C.3})$$

while the transverse metric is given by

$$g_{\perp}^{\mu\nu} = g^{\mu\nu} + z^{\mu} z^{\nu} - t^{\mu} t^{\nu}. \quad (\text{C.4})$$

The vectors z^{μ} and t^{μ} , in the Collins-Soper frame, are defined as

$$z^{\mu} = (\sinh y, \mathbf{0}, \cosh y), \quad t^{\mu} = \frac{q^{\mu}}{Q}, \quad (\text{C.5})$$

and they are such that $z^2 = -1$, $t^2 = 1$ and $(z \cdot q) = 0$. The effect of integrating over the fiducial region in the numerator of eq. (C.1) can be implemented by defining a generalised θ -function, $\Phi(p_1, p_2)$, that is equal to one inside the fiducial region and zero outside. This allows one to integrate also the numerator over the full phase-space of the two outgoing leptons. Next, we integrate out one of the momenta, say p_2 , exploiting the momentum-conservation δ -function:

$$P(q) = \frac{\int d^4 p \delta(p^2) \delta((q-p)^2) \theta(p_0) \theta(q_0 - p_0) L_{\perp}(p, q-p) \Phi(p, q-p)}{\int d^4 p \delta(p^2) \delta((q-p)^2) \theta(p_0) \theta(q_0 - p_0) L_{\perp}(p, q-p)}, \quad (\text{C.6})$$

where we have renamed $p = p_1$. The remaining δ -functions can be used to constrain two of the four components of the momentum p . The first, $\delta(p^2)$, is typically used to set the energy component of p , p_0 , on the mass shell. Since the leptons are massless, this produces

$$\int d^4 p \delta(p^2) \theta(p_0) = \int d^4 p \delta(p_0^2 - |\mathbf{p}|^2) \theta(p_0) = \int \frac{dp_0 d^3 \mathbf{p}}{2|\mathbf{p}|} \delta(p_0 - |\mathbf{p}|) = \int \frac{d^3 \mathbf{p}}{2|\mathbf{p}|}. \quad (\text{C.7})$$

¹¹In eq. (C.1) a parity-violating term is neglected. We will argue in section C.1 that its contribution is negligible for realistic cuts.

Of course, the four-momentum p appearing in the rest of the integrand has to be set on shell ($p_0 = |\mathbf{p}|$). Now we express the three-dimensional measure $d^3\mathbf{p}$ in terms of the transverse momentum \mathbf{p}_T , the pseudo-rapidity η , and the azimuthal angle ϕ of the lepton:

$$\int \frac{d^3\mathbf{p}}{2|\mathbf{p}|} = \int \frac{d|\mathbf{p}_T|^2}{4} d\eta d\phi. \quad (\text{C.8})$$

Now we consider the second δ -function, $\delta((q-p)^2)$, in eq. (C.6). It is convenient to express the vectors q and p in terms of the respective invariant mass, pseudo-rapidity, and transverse momentum:

$$\begin{aligned} q &= (M \cosh y, \mathbf{q}_T, M \sinh y), \\ p &= (|\mathbf{p}_T| \cosh \eta, \mathbf{p}_T, |\mathbf{p}_T| \sinh \eta), \end{aligned} \quad (\text{C.9})$$

with $M = \sqrt{Q^2 + |\mathbf{q}_T|^2}$. Without loss of generality, we assume that the two-dimensional vector \mathbf{q}_T is aligned with the x axis so that $\mathbf{p}_T \cdot \mathbf{q}_T = |\mathbf{p}_T||\mathbf{q}_T| \cos \phi$.¹² This leads to

$$\delta((q-p)^2) = \delta(Q^2 - 2|\mathbf{p}_T|[M \cosh(\eta-y) - |\mathbf{q}_T| \cos \phi]), \quad (\text{C.10})$$

so that

$$\mathcal{P}(q) = \frac{\int \frac{d|\mathbf{p}_T|^2}{4} d\eta d\phi \delta(Q^2 - 2|\mathbf{p}_T|[M \cosh(\eta-y) - |\mathbf{q}_T| \cos \phi]) L_\perp(p, q-p) \Phi(p, q-p)}{\int \frac{d|\mathbf{p}_T|^2}{4} d\eta d\phi \delta(Q^2 - 2|\mathbf{p}_T|[M \cosh(\eta-y) - |\mathbf{q}_T| \cos \phi]) L_\perp(p, q-p)}, \quad (\text{C.11})$$

where the vector p is understood to be on-shell. Now we compute $L_\perp(p, q-p)$ contracting $L_{\mu\nu}$ in eq. (C.3) with the transverse metric $g_\perp^{\mu\nu}$ in eq. (C.4) using eq. (C.9):

$$L_\perp(p, q-p) = 2Q^2 \left[1 + 4 \sinh^2(y-\eta) \frac{|\mathbf{p}_T|^2}{Q^2} \right]. \quad (\text{C.12})$$

We can now integrate out one of the variables in the integrals in eq. (C.11) by making use of the remaining δ -function. Somewhat counterintuitively, it is convenient to integrate over $|\mathbf{p}_T|$. This produces

$$P(q) = \frac{\int_{-\infty}^{\infty} d\eta \int_0^{2\pi} d\phi \left[\frac{2\bar{p}_T^2}{Q^2} + 2 \sinh^2(y-\eta) \frac{\bar{p}_T^4}{Q^4} \right] \Phi(\bar{p}, q-\bar{p})}{\int_{-\infty}^{\infty} d\eta \int_0^{2\pi} d\phi \left[\frac{2\bar{p}_T^2}{Q^2} + 2 \sinh^2(y-\eta) \frac{\bar{p}_T^4}{Q^4} \right]}, \quad (\text{C.13})$$

where \bar{p}_T is defined as

$$\bar{p}_T = \frac{Q^2}{2|\mathbf{q}_T|} \frac{1}{\left[\frac{M \cosh(\eta-y)}{|\mathbf{q}_T|} - \cos \phi \right]}, \quad (\text{C.14})$$

¹²In the general case in which \mathbf{q}_T forms an angle β with the x axis, the scalar product would result in $|\mathbf{p}_T||\mathbf{q}_T| \cos(\phi - \beta)$. However, for observables inclusive in azimuthal angle, the angle β can always be reabsorbed in a redefinition of ϕ .

and \bar{p} symbolises the on-shell vector p with the absolute value of the transverse component set equal to eq. (C.14). Next we turn to consider the integral in ϕ . To this end, the following relation

$$\int_0^{2\pi} d\phi f(\cos \phi) = \int_{-1}^1 \frac{dx}{\sqrt{1-x^2}} [f(x) + f(-x)], \quad (\text{C.15})$$

along with the *indefinite* integrals

$$\int \frac{dx}{(a \pm x)^2 \sqrt{1-x^2}} = \frac{\sqrt{1-x^2}}{(a^2-1)(x \pm a)} \pm \frac{a}{(a^2-1)^{3/2}} \tan^{-1} \left(\frac{1 \pm ax}{\sqrt{a^2-1}\sqrt{1-x^2}} \right), \quad (\text{C.16})$$

and

$$\int \frac{dx}{(a \pm x)^4 \sqrt{1-x^2}} = \frac{\sqrt{1-x^2} [(11a^2+4)x^2 \pm 3a(9a^2+1)x + (18a^4-5a^2+2)]}{6(a^2-1)^3(x \pm a)^3} \pm \frac{a(2a^2+3)}{2(a^2-1)^{7/2}} \tan^{-1} \left(\frac{1 \pm ax}{\sqrt{a^2-1}\sqrt{1-x^2}} \right), \quad (\text{C.17})$$

enable us to compute analytically the primitive function of the integrals in ϕ in eq. (C.13). Eqs. (C.16) and (C.17) are particularly useful because they allow us to compute the integral over ϕ analytically also in the presence of cuts. Let us first compute the integral in the denominator of eq. (C.13), i.e. the integral of L_\perp over the full phase-space. To do so, using eqs. (C.16) and (C.17), we compute the following definite integrals

$$\int_{-1}^1 \frac{dx}{(a \pm x)^2 \sqrt{1-x^2}} = \frac{\pi a}{(a^2-1)^{3/2}}, \quad (\text{C.18})$$

and:

$$\int_{-1}^1 \frac{dx}{(a \pm x)^4 \sqrt{1-x^2}} = \frac{\pi a(2a^2+3)}{2(a^2-1)^{7/2}}. \quad (\text{C.19})$$

Using these results, and finally integrating over η , gives the well-known result

$$\int d^4 p_1 d^4 p_2 \delta(p_1^2) \delta(p_2^2) \theta(p_{1,0}) \theta(p_{2,0}) \delta^{(4)}(p_1 + p_2 - q) L_\perp(p_1, p_2) = \frac{4\pi}{3} Q^2. \quad (\text{C.20})$$

In order to compute the numerator of eq. (C.13), we need to insert the appropriate function Φ . Typically, in DY production the kinematic cuts are imposed independently on the same variables for both the final-state leptons. Therefore, the function Φ factorises into two identical functions acting on each lepton momentum:

$$\Phi(p_1, p_2) = \Theta(p_1) \Theta(p_2). \quad (\text{C.21})$$

We are specifically interested in kinematic cuts on the rapidity and on the transverse momentum of the following kind

$$\eta_{\min} < \eta_{1(2)} < \eta_{\max} \quad \text{and} \quad |\mathbf{p}_{T,1(2)}| > p_{T,\min}. \quad (\text{C.22})$$

Therefore

$$\Theta(p) = \vartheta(\eta - \eta_{\min}) \vartheta(\eta_{\max} - \eta) \vartheta(|\mathbf{p}_T| - p_{T,\min}). \quad (\text{C.23})$$

Using eqs. (C.9) and (C.14) gives

$$\begin{aligned} \Phi(p, q - p) &= \vartheta(\eta - \eta_{\min}) \times \vartheta(\eta_{\max} - \eta) \\ &\quad \times \vartheta(\cos \phi - f^{(2)}(\eta, p_{T,\min})) \\ &\quad \times \vartheta(f^{(3)}(\eta, \eta_{\min}) - \cos \phi) \times \vartheta(f^{(3)}(\eta, \eta_{\max}) - \cos \phi) \\ &\quad \times \vartheta(f^{(4)}(\eta, p_{T,\min}) - \cos \phi), \end{aligned} \tag{C.24}$$

with

$$\begin{aligned} f^{(2)}(\eta, p_{T,\text{cut}}) &= \frac{2Mp_{T,\text{cut}} \cosh(\eta - y) - Q^2}{2p_{T,\text{cut}}|\mathbf{q}_T|}, \\ f^{(3)}(\eta, \eta_{\text{cut}}) &= \frac{M \cosh(\eta - y)}{|\mathbf{q}_T|} - \frac{Q^2 (\sinh(\eta - y) \coth(y - \eta_{\text{cut}}) + \cosh(\eta - y))}{2|\mathbf{q}_T|M}, \\ f^{(4)}(\eta, p_{T,\text{cut}}) &= \frac{M \cosh(\eta - y)(Q^2 - 2p_{T,\text{cut}}^2 + 2|\mathbf{q}_T|^2) - Q^2 \sqrt{M^2 \sinh^2(\eta - y) + p_{T,\text{cut}}^2}}{2|\mathbf{q}_T|(M^2 - p_{T,\text{cut}}^2)}. \end{aligned} \tag{C.25}$$

Now the question is identifying the integration domain on the $(\eta, \cos \phi)$ -plane defined by $\Phi(p, q - p)$ in eq. (C.24). Considering that $-1 \leq \cos \phi \leq 1$, eq. (C.24) can be written in a more convenient way as

$$\begin{aligned} \Phi(p, q - p) &= \vartheta(\eta - \eta_{\min})\vartheta(\eta_{\max} - \eta) \\ &\quad \times \vartheta(\cos \phi - \max[f^{(2)}(\eta, p_{T,\min}), -1]) \\ &\quad \times \vartheta(\min[f^{(3)}(\eta, \eta_{\min}), f^{(3)}(\eta, \eta_{\max}), f^{(4)}(\eta, p_{T,\min}), 1] - \cos \phi). \end{aligned} \tag{C.26}$$

Now we use eq. (C.15) to change $\cos \phi$ into x . This way, the double integral at the numerator of eq. (C.13) reads

$$\int_{-\infty}^{\infty} d\eta \int_{-1}^1 dx \Phi(p, q - p) \cdots = \int_{\eta_{\min}}^{\eta_{\max}} d\eta \vartheta(x_2(\eta) - x_1(\eta)) \int_{x_1(\eta)}^{x_2(\eta)} dx \dots, \tag{C.27}$$

with

$$\begin{aligned} x_1(\eta) &= \max[f^{(2)}(\eta, p_{T,\min}), -1] \\ x_2(\eta) &= \min[f^{(3)}(\eta, \eta_{\min}), f^{(3)}(\eta, \eta_{\max}), f^{(4)}(\eta, p_{T,\min}), 1]. \end{aligned} \tag{C.28}$$

As an example, figure 9 shows the integration domain of the numerator of eq. (C.13) for $p_{T,\min} = 20$ GeV and $-\eta_{\min} = \eta_{\max} = 2.4$ at $Q = 91$ GeV, $|\mathbf{q}_T| = 10$ GeV, and $y = 1$. The grey band corresponds to the region $-1 \leq \cos \phi \leq 1$. The θ -functions in the first line of eq. (C.26) limits the region to the vertical strip defined by $\eta_{\min} < \eta < \eta_{\max}$ (black vertical lines), the θ -function in the second line defines the region above the red line, finally the θ -functions in the third line defines the region below the blue and green lines. The intersection of all regions gives the red-shaded area corresponding to the integration domain.

Gathering all pieces, the final expression for the phase-space reduction factor reads

$$\mathcal{P}(q) = \mathcal{P}(Q, y, q_T) = \int_{\eta_{\min}}^{\eta_{\max}} d\eta \vartheta(x_2(\eta) - x_1(\eta)) [\bar{F}(x_2(\eta), \eta) - \bar{F}(x_1(\eta), \eta)]. \tag{C.29}$$

The function \bar{F} is given by the combination

$$\bar{F}(x, \eta) = \frac{3}{4}F(x, \eta) + \frac{1}{4}G(x, \eta), \quad (\text{C.30})$$

with

$$F(x, \eta) = \frac{1}{4\pi} \frac{Q^2}{E_q^2 - q_T^2} \left\{ \frac{q_T^2 x \sqrt{1-x^2}}{x^2 q_T^2 - E_q^2} - \frac{E_q}{\sqrt{E_q^2 - q_T^2}} \left[\tan^{-1} \left(\frac{q_T - x E_q}{\sqrt{E_q^2 - q_T^2} \sqrt{1-x^2}} \right) - \tan^{-1} \left(\frac{q_T + x E_q}{\sqrt{E_q^2 - q_T^2} \sqrt{1-x^2}} \right) \right] \right\}, \quad (\text{C.31})$$

and

$$G(x, \eta) = \frac{1}{16\pi} \sinh^2(y - \eta) \frac{Q^4}{(E_q^2 - q_T^2)^3} \left\{ \sqrt{1-x^2} q_T \times \left[\frac{(11E_q^2 q_T^2 + 4q_T^4)x^2 + 3E_q q_T (9E_q^2 + q_T^2)x + (18E_q^4 - 5E_q^2 q_T^2 + 2q_T^4)}{(xq_T + E_q)^3} + \frac{(11E_q^2 q_T^2 + 4q_T^4)x^2 - 3E_q q_T (9E_q^2 + q_T^2)x + (18E_q^4 - 5E_q^2 q_T^2 + 2q_T^4)}{(xq_T - E_q)^3} \right] - \frac{6E_q(2E_q^2 + 3q_T^2)}{\sqrt{E_q^2 - q_T^2}} \left[\tan^{-1} \left(\frac{q_T - x E_q}{\sqrt{E_q^2 - q_T^2} \sqrt{1-x^2}} \right) - \tan^{-1} \left(\frac{q_T + x E_q}{\sqrt{E_q^2 - q_T^2} \sqrt{1-x^2}} \right) \right] \right\}, \quad (\text{C.32})$$

where we have defined $E_q = M \cosh(\eta - y)$ and $q_T = |\mathbf{q}_T|$. Interestingly, in the limit $y = q_T = 0$ and assuming $\eta_{\min} = -\eta_{\max}$, \mathcal{P} can be computed analytically. The result is

$$\mathcal{P}(Q, 0, 0) = \vartheta(Q - 2p_{T,\min}) \tanh(\max[\eta_{\max}, \bar{\eta}]) \left[1 - \frac{1}{4 \cosh^2(\max[\eta_{\max}, \bar{\eta}])} \right], \quad (\text{C.33})$$

with $\bar{\eta}$ defined as

$$\bar{\eta} = \cosh^{-1} \left(\frac{Q}{2p_{T,\min}} \right). \quad (\text{C.34})$$

The relation above can be written more explicitly as

$$\mathcal{P}(Q, 0, 0) = \begin{cases} 0 & Q < 2p_{T,\min}, \\ \left(1 - \frac{p_{T,\min}^2}{Q^2} \right) \sqrt{1 - \frac{4p_{T,\min}^2}{Q^2}} & 2p_{T,\min} \leq Q < 2p_{T,\min} \cosh \eta_{\max}, \\ \tanh(\eta_{\max}) \left[1 - \frac{1}{4 \cosh^2(\eta_{\max})} \right] & Q \geq 2p_{T,\min} \cosh \eta_{\max}. \end{cases} \quad (\text{C.35})$$

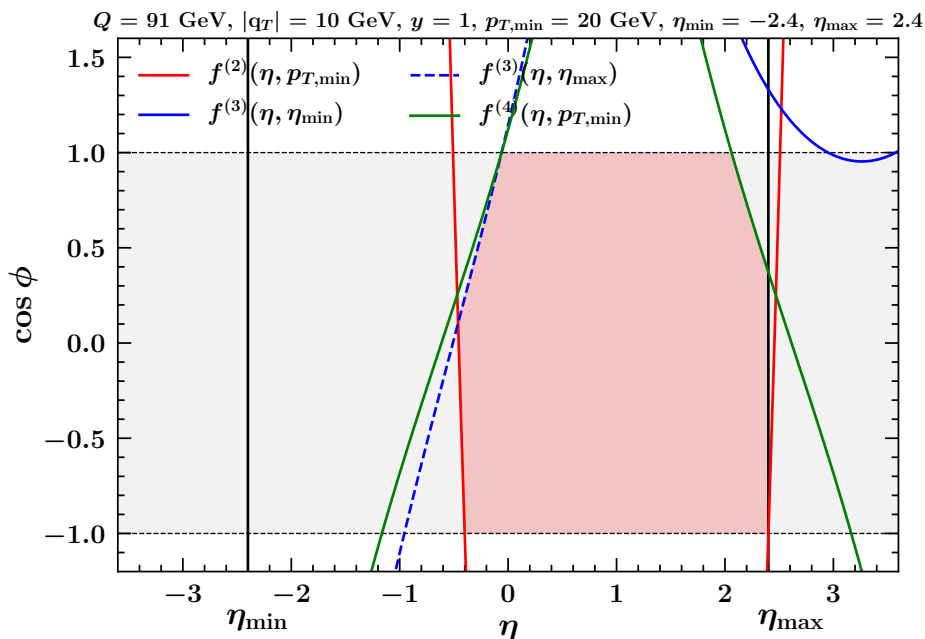


Figure 9. The red area indicates the integration domain of the numerator of the phase-space reduction factor eq. (C.13) for $p_{T,\min} = 20$ GeV and $-\eta_{\min} = \eta_{\max} = 2.4$ at $Q = 91$ GeV, $|\mathbf{q}_T| = 10$ GeV, and $y = 1$.

C.1 Azimuthally-dependent contributions

Azimuthally-dependent modulations disappear in the cross sections if the integration over the azimuthal angle of the virtual boson, Φ , is complete. In the presence of cuts on the final-state leptons, these modulations could generate contributions that were neglected in our analysis, but could be relevant for the description of high-precision data.

We first consider parity-violating effects that generate a $\sin \Phi$ modulation [26]. These contributions stem from interference of the *antisymmetric* contributions to the lepton tensor, proportional to $p_1^\mu p_2^\nu \epsilon_{\mu\nu\rho\sigma}$, and to the hadronic tensor, proportional to $\epsilon_\perp^{\mu\nu}$ defined as

$$\epsilon_\perp^{\mu\nu} \equiv \epsilon^{\mu\nu\rho\sigma} t_\rho z_\sigma, \quad (\text{C.36})$$

where t^μ and z^μ are given in eq. (C.5). Therefore, the contributions we are after result from the contraction of the following Lorentz structures

$$L_{\text{PV}} \equiv p_1^\mu p_2^\nu \epsilon_{\mu\nu\rho\sigma} \epsilon_\perp^{\rho\sigma} = \frac{2|\mathbf{p}_T|^2}{Q} \sinh(y - \eta) [M \cosh(y - \eta) - |\mathbf{q}_T| \cos \phi]. \quad (\text{C.37})$$

Due to the presence of $\sinh(y - \eta)$, eq. (C.37) is such that

$$\int_{-\infty}^{\infty} d\eta L_{\text{PV}} = 0. \quad (\text{C.38})$$

Therefore, for observables inclusive in the lepton phase space, the parity-violating term does not give any contribution. Conversely, the presence of cuts on the final-state leptons may prevent eq. (C.38) from being satisfied, leaving a residual contribution. In order to

quantify this effect, we have taken the same steps performed above to integrate L_{PV} over the fiducial region. It turns out that, for realistic cuts, the numerical size of \mathcal{P}_{PV} relative to the parity-conserving \mathcal{P} is never larger than $\mathcal{O}(10^{-6})$. We conclude that the impact of parity-violating effects in the present analysis is negligible.

Finally, we consider also $\cos \Phi$ modulations, stemming from the following contraction:

$$L_\phi = (z^\mu t^\nu + z^\nu t^\mu) L_{\mu\nu}, \quad (\text{C.39})$$

where the (symmetric part of the) leptonic tensor reads:

$$L^{\mu\nu} = 4(p_1^\mu p_2^\nu + p_2^\mu p_1^\nu - g^{\mu\nu} p_1 p_2). \quad (\text{C.40})$$

We find that

$$L_\phi = 16 \frac{p_T^2}{Q} \sinh(y - \eta) \left[\frac{Q^2}{2p_T} - M \cosh(y - \eta) + q_T \cos \phi \right]. \quad (\text{C.41})$$

Due to the presence of the overall factor $\sinh(y - \eta)$, for relatively central rapidities and for symmetric cuts this term is expected to be very small, in particular to be comparable in size to the parity violating contribution. Moreover, this term would be multiplied by a structure function that has been measured to be small, below 4% in the region of interest here [115].

Open Access. This article is distributed under the terms of the Creative Commons Attribution License ([CC-BY 4.0](https://creativecommons.org/licenses/by/4.0/)), which permits any use, distribution and reproduction in any medium, provided the original author(s) and source are credited.

References

- [1] T.C. Rogers, *An overview of transverse-momentum-dependent factorization and evolution*, *Eur. Phys. J. A* **52** (2016) 153 [[arXiv:1509.04766](https://arxiv.org/abs/1509.04766)] [[INSPIRE](#)].
- [2] M. Diehl, *Introduction to GPDs and TMDs*, *Eur. Phys. J. A* **52** (2016) 149 [[arXiv:1512.01328](https://arxiv.org/abs/1512.01328)] [[INSPIRE](#)].
- [3] R. Angeles-Martinez et al., *Transverse Momentum Dependent (TMD) parton distribution functions: status and prospects*, *Acta Phys. Polon. B* **46** (2015) 2501 [[arXiv:1507.05267](https://arxiv.org/abs/1507.05267)] [[INSPIRE](#)].
- [4] C.T.H. Davies, B.R. Webber and W. Stirling, *Drell-Yan Cross-Sections at Small Transverse Momentum*, [[INSPIRE](#)].
- [5] G.A. Ladinsky and C.P. Yuan, *The Nonperturbative regime in QCD resummation for gauge boson production at hadron colliders*, *Phys. Rev. D* **50** (1994) 4239 [[hep-ph/9311341](https://arxiv.org/abs/hep-ph/9311341)] [[INSPIRE](#)].
- [6] F. Landry, R. Brock, G. Ladinsky and C.P. Yuan, *New fits for the nonperturbative parameters in the CSS resummation formalism*, *Phys. Rev. D* **63** (2001) 013004 [[hep-ph/9905391](https://arxiv.org/abs/hep-ph/9905391)] [[INSPIRE](#)].
- [7] J.-w. Qiu and X.-f. Zhang, *Role of the nonperturbative input in QCD resummed Drell-Yan Q_T distributions*, *Phys. Rev. D* **63** (2001) 114011 [[hep-ph/0012348](https://arxiv.org/abs/hep-ph/0012348)] [[INSPIRE](#)].

- [8] F. Landry, R. Brock, P.M. Nadolsky and C.P. Yuan, *Tevatron Run-1 Z boson data and Collins-Soper-Sterman resummation formalism*, *Phys. Rev. D* **67** (2003) 073016 [[hep-ph/0212159](#)] [[INSPIRE](#)].
- [9] A.V. Konychev and P.M. Nadolsky, *Universality of the Collins-Soper-Sterman nonperturbative function in gauge boson production*, *Phys. Lett. B* **633** (2006) 710 [[hep-ph/0506225](#)] [[INSPIRE](#)].
- [10] T. Becher, M. Neubert and D. Wilhelm, *Electroweak Gauge-Boson Production at Small q_T : Infrared Safety from the Collinear Anomaly*, *JHEP* **02** (2012) 124 [[arXiv:1109.6027](#)] [[INSPIRE](#)].
- [11] S. Camarda et al., *DYTurbo: fast predictions for Drell-Yan processes*, *Eur. Phys. J. C* **80** (2020) 251 [*Erratum ibid.* **80** (2020) 440] [[arXiv:1910.07049](#)] [[INSPIRE](#)].
- [12] R. Meng, F.I. Olness and D.E. Soper, *Semiinclusive deeply inelastic scattering at small $q(T)$* , *Phys. Rev. D* **54** (1996) 1919 [[hep-ph/9511311](#)] [[INSPIRE](#)].
- [13] P.M. Nadolsky, D.R. Stump and C.P. Yuan, *Semiinclusive hadron production at HERA: The Effect of QCD gluon resummation*, *Phys. Rev. D* **61** (2000) 014003 [*Erratum ibid.* **64** (2001) 059903] [[hep-ph/9906280](#)] [[INSPIRE](#)].
- [14] U. D'Alesio, M.G. Echevarria, S. Melis and I. Scimemi, *Non-perturbative QCD effects in q_T spectra of Drell-Yan and Z-boson production*, *JHEP* **11** (2014) 098 [[arXiv:1407.3311](#)] [[INSPIRE](#)].
- [15] I. Scimemi and A. Vladimirov, *Analysis of vector boson production within TMD factorization*, *Eur. Phys. J. C* **78** (2018) 89 [[arXiv:1706.01473](#)] [[INSPIRE](#)].
- [16] V. Bertone, I. Scimemi and A. Vladimirov, *Extraction of unpolarized quark transverse momentum dependent parton distributions from Drell-Yan/Z-boson production*, *JHEP* **06** (2019) 028 [[arXiv:1902.08474](#)] [[INSPIRE](#)].
- [17] A. Signori, A. Bacchetta, M. Radici and G. Schnell, *Investigations into the flavor dependence of partonic transverse momentum*, *JHEP* **11** (2013) 194 [[arXiv:1309.3507](#)] [[INSPIRE](#)].
- [18] M. Anselmino, M. Boglione, J.O. Gonzalez Hernandez, S. Melis and A. Prokudin, *Unpolarised Transverse Momentum Dependent Distribution and Fragmentation Functions from SIDIS Multiplicities*, *JHEP* **04** (2014) 005 [[arXiv:1312.6261](#)] [[INSPIRE](#)].
- [19] M.G. Echevarria, A. Idilbi, Z.-B. Kang and I. Vitev, *QCD Evolution of the Sivers Asymmetry*, *Phys. Rev. D* **89** (2014) 074013 [[arXiv:1401.5078](#)] [[INSPIRE](#)].
- [20] P. Sun, J. Isaacson, C.P. Yuan and F. Yuan, *Nonperturbative functions for SIDIS and Drell-Yan processes*, *Int. J. Mod. Phys. A* **33** (2018) 1841006 [[arXiv:1406.3073](#)] [[INSPIRE](#)].
- [21] A. Bacchetta, F. Delcarro, C. Pisano, M. Radici and A. Signori, *Extraction of partonic transverse momentum distributions from semi-inclusive deep-inelastic scattering, Drell-Yan and Z-boson production*, *JHEP* **06** (2017) 081 [*Erratum ibid.* **06** (2019) 051] [[arXiv:1703.10157](#)] [[INSPIRE](#)].
- [22] I. Scimemi and A. Vladimirov, *Non-perturbative structure of semi-inclusive deep-inelastic and Drell-Yan scattering at small transverse momentum*, *JHEP* **06** (2020) 137 [[arXiv:1912.06532](#)] [[INSPIRE](#)].
- [23] A. Bermudez Martinez et al., *Collinear and TMD parton densities from fits to precision DIS measurements in the parton branching method*, *Phys. Rev. D* **99** (2019) 074008 [[arXiv:1804.11152](#)] [[INSPIRE](#)].

- [24] A. Bermudez Martinez et al., *Production of Z-bosons in the parton branching method*, *Phys. Rev. D* **100** (2019) 074027 [[arXiv:1906.00919](#)] [[INSPIRE](#)].
- [25] A. Bacchetta, G. Bozzi, M. Radici, M. Ritzmann and A. Signori, *Effect of Flavor-Dependent Partonic Transverse Momentum on the Determination of the W Boson Mass in Hadronic Collisions*, *Phys. Lett. B* **788** (2019) 542 [[arXiv:1807.02101](#)] [[INSPIRE](#)].
- [26] D. Boer, *Investigating the origins of transverse spin asymmetries at RHIC*, *Phys. Rev. D* **60** (1999) 014012 [[hep-ph/9902255](#)] [[INSPIRE](#)].
- [27] J. Collins, *Foundations of perturbative QCD*, vol. 32, Cambridge University Press (11, 2013) [[INSPIRE](#)].
- [28] J.C. Collins and D.E. Soper, *Back-To-Back Jets in QCD*, *Nucl. Phys. B* **193** (1981) 381 [*Erratum ibid.* **213** (1983) 545] [[INSPIRE](#)].
- [29] J.-y. Chiu, A. Jain, D. Neill and I.Z. Rothstein, *The Rapidity Renormalization Group*, *Phys. Rev. Lett.* **108** (2012) 151601 [[arXiv:1104.0881](#)] [[INSPIRE](#)].
- [30] J.-Y. Chiu, A. Jain, D. Neill and I.Z. Rothstein, *A Formalism for the Systematic Treatment of Rapidity Logarithms in Quantum Field Theory*, *JHEP* **05** (2012) 084 [[arXiv:1202.0814](#)] [[INSPIRE](#)].
- [31] I. Scimemi and A. Vladimirov, *Systematic analysis of double-scale evolution*, *JHEP* **08** (2018) 003 [[arXiv:1803.11089](#)] [[INSPIRE](#)].
- [32] G. Billis, F.J. Tackmann and J. Talbert, *Higher-Order Sudakov Resummation in Coupled Gauge Theories*, *JHEP* **03** (2020) 182 [[arXiv:1907.02971](#)] [[INSPIRE](#)].
- [33] W. Bizoń et al., *Fiducial distributions in Higgs and Drell-Yan production at $N^3LL + NNLO$* , *JHEP* **12** (2018) 132 [[arXiv:1805.05916](#)] [[INSPIRE](#)].
- [34] J. Collins and T.C. Rogers, *Connecting Different TMD Factorization Formalisms in QCD*, *Phys. Rev. D* **96** (2017) 054011 [[arXiv:1705.07167](#)] [[INSPIRE](#)].
- [35] S. Catani, L. Cieri, D. de Florian, G. Ferrera and M. Grazzini, *Vector boson production at hadron colliders: hard-collinear coefficients at the NNLO*, *Eur. Phys. J. C* **72** (2012) 2195 [[arXiv:1209.0158](#)] [[INSPIRE](#)].
- [36] M.G. Echevarria, I. Scimemi and A. Vladimirov, *Unpolarized Transverse Momentum Dependent Parton Distribution and Fragmentation Functions at next-to-next-to-leading order*, *JHEP* **09** (2016) 004 [[arXiv:1604.07869](#)] [[INSPIRE](#)].
- [37] M.-x. Luo, T.-Z. Yang, H.X. Zhu and Y.J. Zhu, *Quark Transverse Parton Distribution at the Next-to-Next-to-Next-to-Leading Order*, *Phys. Rev. Lett.* **124** (2020) 092001 [[arXiv:1912.05778](#)] [[INSPIRE](#)].
- [38] Y. Li and H.X. Zhu, *Bootstrapping Rapidity Anomalous Dimensions for Transverse-Momentum Resummation*, *Phys. Rev. Lett.* **118** (2017) 022004 [[arXiv:1604.01404](#)] [[INSPIRE](#)].
- [39] J. Davies, A. Vogt, B. Ruijl, T. Ueda and J.A.M. Vermaseren, *Large- N_f contributions to the four-loop splitting functions in QCD*, *Nucl. Phys. B* **915** (2017) 335 [[arXiv:1610.07477](#)] [[INSPIRE](#)].
- [40] S. Moch, B. Ruijl, T. Ueda, J.A.M. Vermaseren and A. Vogt, *Four-Loop Non-Singlet Splitting Functions in the Planar Limit and Beyond*, *JHEP* **10** (2017) 041 [[arXiv:1707.08315](#)] [[INSPIRE](#)].

- [41] S. Moch, B. Ruijl, T. Ueda, J.A.M. Vermaseren and A. Vogt, *On quartic colour factors in splitting functions and the gluon cusp anomalous dimension*, *Phys. Lett. B* **782** (2018) 627 [[arXiv:1805.09638](#)] [[INSPIRE](#)].
- [42] I.W. Stewart, F.J. Tackmann, J.R. Walsh and S. Zuberi, *Jet p_T resummation in Higgs production at NNLL' + NNLO*, *Phys. Rev. D* **89** (2014) 054001 [[arXiv:1307.1808](#)] [[INSPIRE](#)].
- [43] M.A. Ebert and F.J. Tackmann, *Resummation of Transverse Momentum Distributions in Distribution Space*, *JHEP* **02** (2017) 110 [[arXiv:1611.08610](#)] [[INSPIRE](#)].
- [44] S. Catani, *Higher order QCD corrections in hadron collisions: Soft gluon resummation and exponentiation*, [hep-ph/9610413](#) [[INSPIRE](#)].
- [45] G. Bozzi, S. Catani, G. Ferrera, D. de Florian and M. Grazzini, *Production of Drell-Yan lepton pairs in hadron collisions: Transverse-momentum resummation at next-to-next-to-leading logarithmic accuracy*, *Phys. Lett. B* **696** (2011) 207 [[arXiv:1007.2351](#)] [[INSPIRE](#)].
- [46] T. Becher, M. Neubert and D. Wilhelm, *Higgs-Boson Production at Small Transverse Momentum*, *JHEP* **05** (2013) 110 [[arXiv:1212.2621](#)] [[INSPIRE](#)].
- [47] A. Banfi, H. McAslan, P.F. Monni and G. Zanderighi, *The two-jet rate in e^+e^- at next-to-next-to-leading-logarithmic order*, *Phys. Rev. Lett.* **117** (2016) 172001 [[arXiv:1607.03111](#)] [[INSPIRE](#)].
- [48] G. Bozzi, S. Catani, D. de Florian and M. Grazzini, *Transverse-momentum resummation and the spectrum of the Higgs boson at the LHC*, *Nucl. Phys. B* **737** (2006) 73 [[hep-ph/0508068](#)] [[INSPIRE](#)].
- [49] S. Catani, L. Cieri, D. de Florian, G. Ferrera and M. Grazzini, *Universality of transverse-momentum resummation and hard factors at the NNLO*, *Nucl. Phys. B* **881** (2014) 414 [[arXiv:1311.1654](#)] [[INSPIRE](#)].
- [50] C. Muselli, S. Forte and G. Ridolfi, *Combined threshold and transverse momentum resummation for inclusive observables*, *JHEP* **03** (2017) 106 [[arXiv:1701.01464](#)] [[INSPIRE](#)].
- [51] S. Alioli, A. Broggio, S. Kallweit, M.A. Lim and L. Rottoli, *Higgsstrahlung at NNLL' + NNLO matched to parton showers in GENEVA*, *Phys. Rev. D* **100** (2019) 096016 [[arXiv:1909.02026](#)] [[INSPIRE](#)].
- [52] M.G. Echevarria, T. Kasemets, J.-P. Lansberg, C. Pisano and A. Signori, *Matching factorization theorems with an inverse-error weighting*, *Phys. Lett. B* **781** (2018) 161 [[arXiv:1801.01480](#)] [[INSPIRE](#)].
- [53] G. Lustermans, J.K.L. Michel, F.J. Tackmann and W.J. Waalewijn, *Joint two-dimensional resummation in q_T and 0-jettiness at NNLL*, *JHEP* **03** (2019) 124 [[arXiv:1901.03331](#)] [[INSPIRE](#)].
- [54] L.A. Harland-Lang, A.D. Martin, P. Motylinski and R.S. Thorne, *Parton distributions in the LHC era: MMHT 2014 PDFs*, *Eur. Phys. J. C* **75** (2015) 204 [[arXiv:1412.3989](#)] [[INSPIRE](#)].
- [55] A. Buckley et al., *LHAPDF6: parton density access in the LHC precision era*, *Eur. Phys. J. C* **75** (2015) 132 [[arXiv:1412.7420](#)] [[INSPIRE](#)].
- [56] S. Catani, M.L. Mangano, P. Nason and L. Trentadue, *The Resummation of soft gluons in hadronic collisions*, *Nucl. Phys. B* **478** (1996) 273 [[hep-ph/9604351](#)] [[INSPIRE](#)].

- [57] J.C. Collins, D.E. Soper and G.F. Sterman, *Transverse Momentum Distribution in Drell-Yan Pair and W and Z Boson Production*, *Nucl. Phys. B* **250** (1985) 199 [INSPIRE].
- [58] J. Collins, L. Gamberg, A. Prokudin, T.C. Rogers, N. Sato and B. Wang, *Relating Transverse Momentum Dependent and Collinear Factorization Theorems in a Generalized Formalism*, *Phys. Rev. D* **94** (2016) 034014 [arXiv:1605.00671] [INSPIRE].
- [59] M. Burkardt and B. Pasquini, *Modelling the nucleon structure*, *Eur. Phys. J. A* **52** (2016) 161 [arXiv:1510.02567] [INSPIRE].
- [60] D. Müller and D.S. Hwang, *The concept of phenomenological light-front wave functions — Regge improved diquark model predictions*, arXiv:1407.1655 [INSPIRE].
- [61] HERMES collaboration, *Multiplicities of charged pions and kaons from semi-inclusive deep-inelastic scattering by the proton and the deuteron*, *Phys. Rev. D* **87** (2013) 074029 [arXiv:1212.5407] [INSPIRE].
- [62] COMPASS collaboration, *Transverse-momentum-dependent Multiplicities of Charged Hadrons in Muon-Deuteron Deep Inelastic Scattering*, *Phys. Rev. D* **97** (2018) 032006 [arXiv:1709.07374] [INSPIRE].
- [63] G. Bozzi and A. Signori, *Nonperturbative Uncertainties on the Transverse Momentum Distribution of Electroweak Bosons and on the Determination of the Boson Mass at the LHC*, *Adv. High Energy Phys.* **2019** (2019) 2526897 [arXiv:1901.01162] [INSPIRE].
- [64] A. Bacchetta, F. Conti and M. Radici, *Transverse-momentum distributions in a diquark spectator model*, *Phys. Rev. D* **78** (2008) 074010 [arXiv:0807.0323] [INSPIRE].
- [65] M. Wakamatsu, *Transverse momentum distributions of quarks in the nucleon from the Chiral Quark Soliton Model*, *Phys. Rev. D* **79** (2009) 094028 [arXiv:0903.1886] [INSPIRE].
- [66] A.V. Efremov, P. Schweitzer, O.V. Teryaev and P. Zavada, *The relation between TMDs and PDFs in the covariant parton model approach*, *Phys. Rev. D* **83** (2011) 054025 [arXiv:1012.5296] [INSPIRE].
- [67] C. Bourrely, F. Buccella and J. Soffer, *Semiinclusive DIS cross sections and spin asymmetries in the quantum statistical parton distributions approach*, *Phys. Rev. D* **83** (2011) 074008 [arXiv:1008.5322] [INSPIRE].
- [68] H.H. Matevosyan, W. Bentz, I.C. Cloet and A.W. Thomas, *Transverse Momentum Dependent Fragmentation and Quark Distribution Functions from the NJL-jet Model*, *Phys. Rev. D* **85** (2012) 014021 [arXiv:1111.1740] [INSPIRE].
- [69] P. Schweitzer, M. Strikman and C. Weiss, *Intrinsic transverse momentum and parton correlations from dynamical chiral symmetry breaking*, *JHEP* **01** (2013) 163 [arXiv:1210.1267] [INSPIRE].
- [70] B.U. Musch, P. Hagler, J.W. Negele and A. Schafer, *Exploring quark transverse momentum distributions with lattice QCD*, *Phys. Rev. D* **83** (2011) 094507 [arXiv:1011.1213] [INSPIRE].
- [71] A. Bacchetta and M.G. Echevarria, *QCD×QED evolution of TMDs*, *Phys. Lett. B* **788** (2019) 280 [arXiv:1810.02297] [INSPIRE].
- [72] L. Cieri, G. Ferrera and G.F.R. Sborlini, *Combining QED and QCD transverse-momentum resummation for Z boson production at hadron colliders*, *JHEP* **08** (2018) 165 [arXiv:1805.11948] [INSPIRE].
- [73] O. Lupton and M. Vesterinen, *Simultaneously determining the W^\pm boson mass and parton shower model parameters*, arXiv:1907.09958 [INSPIRE].

- [74] R.-b. Meng, F.I. Olness and D.E. Soper, *Semiinclusive deeply inelastic scattering at electron-proton colliders*, *Nucl. Phys. B* **371** (1992) 79 [INSPIRE].
- [75] C.A. Aidala, B. Field, L.P. Gamberg and T.C. Rogers, *Limits on transverse momentum dependent evolution from semi-inclusive deep inelastic scattering at moderate Q* , *Phys. Rev. D* **89** (2014) 094002 [arXiv:1401.2654] [INSPIRE].
- [76] Z.-B. Kang, A. Prokudin, P. Sun and F. Yuan, *Extraction of Quark Transversity Distribution and Collins Fragmentation Functions with QCD Evolution*, *Phys. Rev. D* **93** (2016) 014009 [arXiv:1505.05589] [INSPIRE].
- [77] J. Collins and T. Rogers, *Understanding the large-distance behavior of transverse-momentum-dependent parton densities and the Collins-Soper evolution kernel*, *Phys. Rev. D* **91** (2015) 074020 [arXiv:1412.3820] [INSPIRE].
- [78] M.A. Ebert, I.W. Stewart and Y. Zhao, *Determining the Nonperturbative Collins-Soper Kernel From Lattice QCD*, *Phys. Rev. D* **99** (2019) 034505 [arXiv:1811.00026] [INSPIRE].
- [79] G. Moreno et al., *Dimuon production in proton-copper collisions at $\sqrt{s} = 38.8$ -GeV*, *Phys. Rev. D* **43** (1991) 2815 [INSPIRE].
- [80] A.S. Ito et al., *Measurement of the Continuum of Dimuons Produced in High-Energy Proton-Nucleus Collisions*, *Phys. Rev. D* **23** (1981) 604 [INSPIRE].
- [81] CDF collaboration, *The transverse momentum and total cross section of e^+e^- pairs in the Z boson region from $p\bar{p}$ collisions at $\sqrt{s} = 1.8$ TeV*, *Phys. Rev. Lett.* **84** (2000) 845 [hep-ex/0001021] [INSPIRE].
- [82] CDF collaboration, *Transverse momentum cross section of e^+e^- pairs in the Z -boson region from $p\bar{p}$ collisions at $\sqrt{s} = 1.96$ TeV*, *Phys. Rev. D* **86** (2012) 052010 [arXiv:1207.7138] [INSPIRE].
- [83] D0 collaboration, *Measurement of the inclusive differential cross section for Z bosons as a function of transverse momentum in $p\bar{p}$ collisions at $\sqrt{s} = 1.8$ TeV*, *Phys. Rev. D* **61** (2000) 032004 [hep-ex/9907009] [INSPIRE].
- [84] D0 collaboration, *Measurement of the shape of the boson transverse momentum distribution in $p\bar{p} \rightarrow Z/\gamma^* \rightarrow e^+e^- + X$ events produced at $\sqrt{s} = 1.96$ -TeV*, *Phys. Rev. Lett.* **100** (2008) 102002 [arXiv:0712.0803] [INSPIRE].
- [85] D0 collaboration, *Measurement of the Normalized $Z/\gamma^* \rightarrow \mu^+\mu^-$ Transverse Momentum Distribution in $p\bar{p}$ Collisions at $\sqrt{s} = 1.96$ TeV*, *Phys. Lett. B* **693** (2010) 522 [arXiv:1006.0618] [INSPIRE].
- [86] LHCb collaboration, *Measurement of the forward Z boson production cross-section in pp collisions at $\sqrt{s} = 7$ TeV*, *JHEP* **08** (2015) 039 [arXiv:1505.07024] [INSPIRE].
- [87] LHCb collaboration, *Measurement of forward W and Z boson production in pp collisions at $\sqrt{s} = 8$ TeV*, *JHEP* **01** (2016) 155 [arXiv:1511.08039] [INSPIRE].
- [88] CMS collaboration, *Measurement of the Rapidity and Transverse Momentum Distributions of Z Bosons in pp Collisions at $\sqrt{s} = 7$ TeV*, *Phys. Rev. D* **85** (2012) 032002 [arXiv:1110.4973] [INSPIRE].
- [89] CMS collaboration, *Measurement of the transverse momentum spectra of weak vector bosons produced in proton-proton collisions at $\sqrt{s} = 8$ TeV*, *JHEP* **02** (2017) 096 [arXiv:1606.05864] [INSPIRE].

- [90] ATLAS collaboration, *Measurement of the transverse momentum and ϕ_{η}^* distributions of Drell-Yan lepton pairs in proton-proton collisions at $\sqrt{s} = 8$ TeV with the ATLAS detector*, *Eur. Phys. J. C* **76** (2016) 291 [[arXiv:1512.02192](#)] [[INSPIRE](#)].
- [91] PHENIX collaboration, *Measurements of $\mu\mu$ pairs from open heavy flavor and Drell-Yan in $p + p$ collisions at $\sqrt{s} = 200$ GeV*, *Phys. Rev. D* **99** (2019) 072003 [[arXiv:1805.02448](#)] [[INSPIRE](#)].
- [92] LHCb collaboration, *Measurement of the forward Z boson production cross-section in pp collisions at $\sqrt{s} = 13$ TeV*, *JHEP* **09** (2016) 136 [[arXiv:1607.06495](#)] [[INSPIRE](#)].
- [93] ATLAS collaboration, *Measurement of the Z/ γ^* boson transverse momentum distribution in pp collisions at $\sqrt{s} = 7$ TeV with the ATLAS detector*, *JHEP* **09** (2014) 145 [[arXiv:1406.3660](#)] [[INSPIRE](#)].
- [94] S. Catani and M. Grazzini, *An NNLO subtraction formalism in hadron collisions and its application to Higgs boson production at the LHC*, *Phys. Rev. Lett.* **98** (2007) 222002 [[hep-ph/0703012](#)] [[INSPIRE](#)].
- [95] S. Catani, L. Cieri, G. Ferrera, D. de Florian and M. Grazzini, *Vector boson production at hadron colliders: a fully exclusive QCD calculation at NNLO*, *Phys. Rev. Lett.* **103** (2009) 082001 [[arXiv:0903.2120](#)] [[INSPIRE](#)].
- [96] G. D’Agostini, *On the use of the covariance matrix to fit correlated data*, *Nucl. Instrum. Meth. A* **346** (1994) 306 [[INSPIRE](#)].
- [97] G. D’Agostini, *Bayesian reasoning in data analysis: A critical introduction*, World Scientific (2003) [[INSPIRE](#)].
- [98] R.D. Ball et al., *Parton Distribution Benchmarking with LHC Data*, *JHEP* **04** (2013) 125 [[arXiv:1211.5142](#)] [[INSPIRE](#)].
- [99] NNPDF collaboration, *Fitting Parton Distribution Data with Multiplicative Normalization Uncertainties*, *JHEP* **05** (2010) 075 [[arXiv:0912.2276](#)] [[INSPIRE](#)].
- [100] COMPASS collaboration, *Hadron Transverse Momentum Distributions in Muon Deep Inelastic Scattering at 160 GeV/c*, *Eur. Phys. J. C* **73** (2013) 2531 [Erratum *ibid.* **75** (2015) 94] [[arXiv:1305.7317](#)] [[INSPIRE](#)].
- [101] J. Dudek et al., *Physics Opportunities with the 12 GeV Upgrade at Jefferson Lab*, *Eur. Phys. J. A* **48** (2012) 187 [[arXiv:1208.1244](#)] [[INSPIRE](#)].
- [102] D. Boer et al., *Gluons and the quark sea at high energies: Distributions, polarization, tomography*, [arXiv:1108.1713](#) [[INSPIRE](#)].
- [103] A. Accardi et al., *Electron Ion Collider: The Next QCD Frontier: Understanding the glue that binds us all*, *Eur. Phys. J. A* **52** (2016) 268 [[arXiv:1212.1701](#)] [[INSPIRE](#)].
- [104] V. Bertone, S. Carrazza and J. Rojo, *APFEL: A PDF Evolution Library with QED corrections*, *Comput. Phys. Commun.* **185** (2014) 1647 [[arXiv:1310.1394](#)] [[INSPIRE](#)].
- [105] V. Bertone, *APFEL++: A new PDF evolution library in C++*, *PoS DIS2017* (2018) 201 [[arXiv:1708.00911](#)] [[INSPIRE](#)].
- [106] T. Kluge, K. Rabbertz and M. Wobisch, *FastNLO: Fast pQCD calculations for PDF fits*, in *14th International Workshop on Deep Inelastic Scattering*, pp. 483–486 (2006) [[DOI](#)] [[hep-ph/0609285](#)] [[INSPIRE](#)].

- [107] FASTNLO collaboration, *New features in version 2 of the fastNLO project*, in *20th International Workshop on Deep-Inelastic Scattering and Related Subjects*, pp. 217–221 (2012) [DOI] [arXiv:1208.3641] [INSPIRE].
- [108] T. Carli et al., *A posteriori inclusion of parton density functions in NLO QCD final-state calculations at hadron colliders: The APPLGRID Project*, *Eur. Phys. J. C* **66** (2010) 503 [arXiv:0911.2985] [INSPIRE].
- [109] F. James, *MINUIT Function Minimization and Error Analysis: Reference Manual Version 94.1*, CERN-D-506 (1994) [INSPIRE].
- [110] S. Agarwal, K. Mierle and Others, *Ceres solver*, <http://ceres-solver.org>.
- [111] S. Alekhin et al., *HERAFitter*, *Eur. Phys. J. C* **75** (2015) 304 [arXiv:1410.4412] [INSPIRE].
- [112] xFitter web page, <https://www.xfitter.org/xFitter/>.
- [113] E. Maguire, L. Heinrich and G. Watt, *HEPData: a repository for high energy physics data*, *J. Phys. Conf. Ser.* **898** (2017) 102006 [arXiv:1704.05473] [INSPIRE].
- [114] F. Hautmann et al., *TMDlib and TMDplotter: library and plotting tools for transverse-momentum-dependent parton distributions*, *Eur. Phys. J. C* **74** (2014) 3220 [arXiv:1408.3015] [INSPIRE].
- [115] ATLAS collaboration, *Measurement of the angular coefficients in Z-boson events using electron and muon pairs from data taken at $\sqrt{s} = 8$ TeV with the ATLAS detector*, *JHEP* **08** (2016) 159 [arXiv:1606.00689] [INSPIRE].